RISØ

Risø-R-701(EN)

The Boundary Layer of Mars: Fluxes, Stability, Turbulent Spectra and Growth of the Mixed Layer

Lars Landberg, Søren E. Larsen
Dept. of Meteorology and Wind Energy
Risø National Laboratory

James E. Tillman
Dept. of Atmospheric Sciences
University of Washington

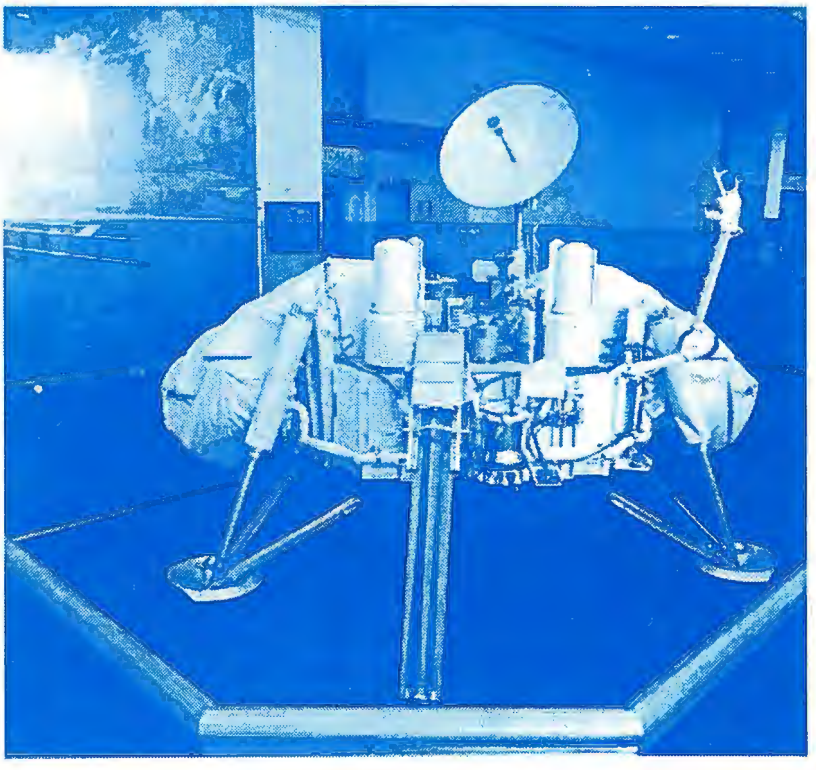

Risø National Laboratory, Roskilde, Denmark
September 1995

Intentionally left blank

Risø–R–701(EN)

The Boundary Layer of Mars: Fluxes, Stability, Turbulent Spectra and Growth of the Mixed Layer

Lars Landberg, Søren E. Larsen
Dept. of Meteorology and Wind Energy
Risø National Laboratory

James E. Tillman
Dept. of Atmospheric Sciences
University of Washington

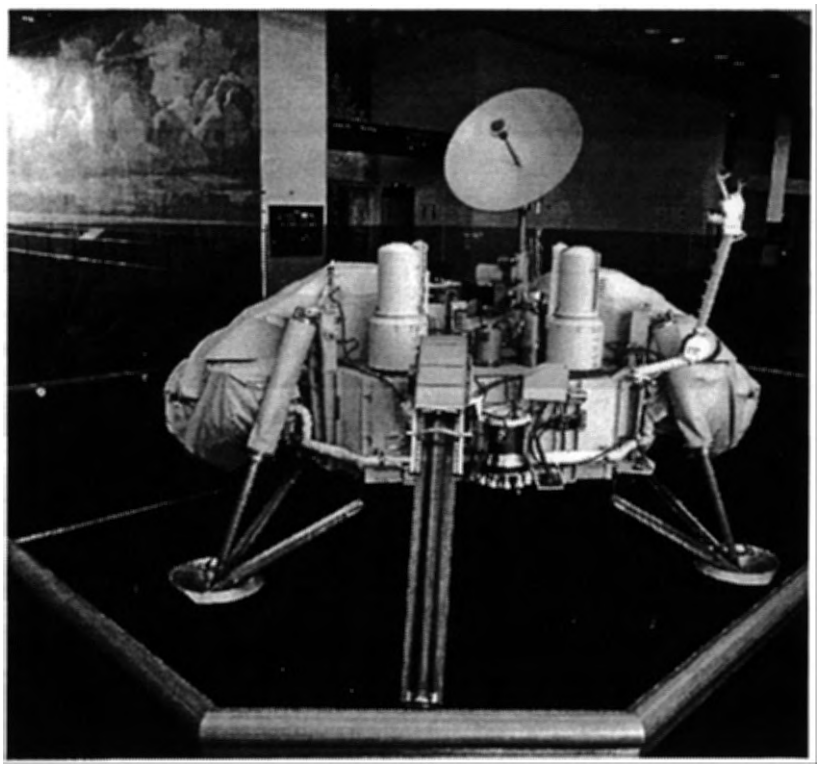

Risø National Laboratory, Roskilde, Denmark
September 1995

Abstract Spectra of wind, from high frequency measurements in the Martian atmospheric surface layer, along with the diurnal variation of the height of the mixed atmospheric surface layer are estimated. Heat and momentum fluxes, and stability, are calculated for early spring, from estimates of the surface temperature and from mean Viking Lander 2 temperatures and winds at 44° N, using similarity theory. The surface temperature estimates are obtained from Mission Operations software, enhanced to improve the sensor temperature measurements. Flow distortion by the lander is also taken into account. The diurnal variation of the mechanically and convectively mixed planetary boundary layer is estimated and sample values are presented. The spectra are compared with model spectra, which have been adjusted to simulate aliasing, and high frequency roll-off, both due to sensor response and the large Kolmorogov length of Mars. The surface layer parameters, including the depth of the mixed layer, are used in the calculation of the model spectra for three surface roughnesses and two measuring heights. The spectral models depend on the surface parameters and the estimated surface temperature, and their agreement with the calculated spectra indicates that the surface layer estimation techniques produce self consistent estimates, both for day and night conditions. This agreement is in spite of the fact that an inertial subrange is virtually absent in the Martian atmospheric surface layer due to the large Kolmogorov length scale. The results show that similarity theory developed for Earth applies to Mars, that the spectral models are universal, and can be applied at heights lower by a factor of three than in prior terrestrial applications. They also demonstrate that it is possible to estimate the effects of severe aliasing of wind measurements, and filtering by sensor and atmospheric processes, to produce a model which agrees well with the measured spectra. These results suggest that z_0 probably lies between 1.0 and 3.0 cm and that the value can be significantly refined by further analyses. Parts of the findings in this report have been published in Tillman et al, 1994.

Cover: The Viking Lander, located in the Smithsonian National Air and Space Museum, Washington DC, is one of the four landers built by Martin Marietta for the 1975 Viking Mission to Mars program which was directed by NASA Langley Research Center. Two landers are on the surface of Mars while this photo shows the Proof Test Capsule, PTC, Lander. The PTC was used at Martin Marietta to verify the functionality of the lander systems, sensors and components, including exposure to launch, space and Mars like environmental stresses and to verify flight software changes and sequences during the mission operations. The Meteorology Sensor Assembly can be found on the white Meteorology boom to the right of the S band antenna in the upper right part of the photograph. Photo: Copyright Bill Guest.

IBSN 87–550–1915–3
ISSN 0106–2840

Grafisk Service · Risø · 1995

Contents

List of Figures

List of Tables

1 Introduction

During the Viking Mission to the planet Mars, two Landers, Viking Lander 1, VL-1, 22° N, 48° W, and Lander 2, VL-2, 48° N, 225° W were landed on the surface of Mars. The landed Meteorology Experiment was designed to measure pressure, temperature, wind speed and wind direction in the atmospheric surface layer for a minimum of 90 Martian days, sols. The goal was to collect and analyze the diurnal, seasonal and annual variation over one Mars year, 669 sols, and to collect limited segments at high sampling rates to study the turbulent properties of the surface layer. The Viking Meteorology Instrument System, VMIS, consisted of temperature and wind sensors, pressure was measured by an engineering sensor and all were made at a nominal height of 1.61 metres. The pressure measurement was made from a sensor inside the lander and ventilated to the atmosphere: its location and height are of little consequence to the investigation. By taking over the processing of the complete raw spacecraft mission data stream later in the mission, one of us (Tillman) was able to provide the mission operations spacecraft engineering processing for Jet Propulsion Laboratory and continue science acquisition and processing to allow the extension of the mission for an additional 1,200 sols until sol 2,245 when VL-1 failed.

Measurements of temperature and winds from the VL-2 VMIS, along with inferred surface temperatures, have been used to calculate spectra and compare them with model spectra adapted from terrestrial models. These are used in turn to infer a range of possible aerodynamic roughness lengths and effective measuring heights, the latter taking into account flow distortion by the lander. Stability, heat and momentum fluxes are calculated from mean wind and temperature, and inferred surface temperatures. These parameters were then used to determine the height of the inversion for unstable daytime conditions during two seasons and to compute model spectra for the longitudinal and lateral winds. These model wind and temperature spectra are compared with the measured Martian spectra to determine some characteristics of the boundary layer of Mars and the extent to which it is behaving like that of the Earth.

2 Mars

A brief introduction to the planet Mars is followed by a description of the atmosphere, its annual variations and the conditions surrounding the seasons for these boundary layer analyses.

2.1 The planet

Mars is the first of the outer planets, its mean distance from the sun is 227.9×10^6 km, and its diameter about half the size of the Earth's (cf. Table 1). A martian day, called a 'sol ', is 24 hours 39 minutes and 35 seconds. The polar regions have CO_2 ice caps of varying size during the year. Although features resembling dried-up river beds are stretched across the surface, indicating that there has been liquid water at the surface during earlier periods with a milder and more moist climate, the temperatures are too cold and the pressure too low to allow liquid water anywhere at the surface in the present epoch. The surface near the landers is covered by small and large stones with the intervening areas covered by dust deposited during the global dust storms, Arvidson *et al.* (1982).

Table 1. Astronomical data for Mars and the Earth.

	Mars	Earth
Mean distance (AE)	1.5237	1.0000
Mean distance (10^6 km)	227.94	149.60
Eccentricity	0.0934	0.0167
Obliquity of the ecliptic	1.50°	-
Siderian period of revolution (Earth days)	686.980	365.256
Equatorial diameter (km)	6,794	12,756
Polar diameter (km)	6,759	12,714
Period of rotation (hours)	24.62	23.93
Mass (kg)	6.4191×10^{23}	5.9742×10^{24}
Density (10^3 kg m^{-3})	3.94	5.52

2.2 The atmosphere

The atmosphere consists of 95%CO_2 (cf. Table 2), some of which condenses in the winter polar region and sublimates during the rest of the year, causing seasonal variations in the atmospheric pressure of approximately ±15% at both lander sites. The mean pressure is 6–7 mb, but varies from 9 mb at the lowest elevations to only 1 mb at the top of the great volcanos. The axis of revolution of Mars is at an angle of 23.59° with the planet's orbit around the Sun, while for Earth the value is 23.44°. Normally, this would mean that the seasons on Mars are very like those of Earth. However, the far greater eccentricity of the Martian orbit, 0.0934, compared with that of Earth, 0.0167 (cf. Table 1), produces much larger differences between the winter (or summer) seasons meteorology in each hemisphere on Mars than on Earth: Mars receives 45% more solar radiation at perihelion[1] than when it is at aphelion[2]. The magnitude of this orbital eccentricity can best be illustrated by the annual cycle of pressure due to condensation and sublimation of CO_2 during winter in the polar regions. With a mean pressure of approximately 9.38 millibars at VL-1 during the second, less dusty, year, the minimum pressure due to condensation on the northern polar cap and sublimation in the northern hemisphere during winter is 8.0 millibars while the value observed at VL-1 during the corresponding southern hemisphere winter is 7.16 millibars!

Table 2. Composition of the martian atmosphere (From Owen et al., *1977).*

CO_2	95.32 %	H_2O	0.03 %
N_2	2.70 %	Ne	2.50 ppm
Ar	1.60 %	Kr	0.30 ppm
O_2	0.13 %	Xe	0.08 ppm
CO	0.07 %	O_3	0.03 ppm

CO_2 as well as water ice clouds are present. In the winter polar regions, a dense water ice cloud layer is present at and near the poles while surface based fog and mist are also found in the early hours in the morning in the deep ravines. The

[1] Perihelion is the orbital position closest to the sun.
[2] Aphelion is the orbital position furthest away from the sun.

vertically integrated column water vapor varies from a few to a maximum of 100 precipitable microns, the latter during late summer at northern high latitudes.

At VL-1, the sol mean temperatures vary between 195 and 215 K during the year while for VL-2 the values are 160 to 220 K. Excluding the wind directions for which there is lander interference, which may bias the results, the hourly average minimum for temperature for VL1 is 172 K while the maximum is 250 K; for VL-2 the values are 157 and 248 K respectively. Global dust storms cover the planet to depths of up to 50 km for periods of months during some, but not other, years, Colburn *et al.* (1989), Tillman (1988), and Zurek *et al.* (1991). Diurnal temperature variations range between a few degrees at VL-2 during winter, to slightly more than 60 K at VL-1 during late summer, Ryan and Henry (1979).

Analyses of the wind, temperature and pressure at VL-2 indicate that baroclinic perturbations of the zonal mean flow on Mars exist and the similarities and differences between terrestrial and Martian baroclinic activity have been described by Tillman *et al.* (1988), Barnes (1984), Leovy *et al.* (1985), and Murphy *et al.* (1991). During early summer, the diurnal patterns of variation of wind at the the VL-1 and VL-2 sites are quite different (Hess *et al.*, 1977). VL-1 has a counterclockwise rotation with one complete rotation per sol while at VL-2, the wind behaved differently : 1) the wind rotates clockwise, 2) all wind directions are represented and 3) the wind speed is significantly less than at the VL-1 site. More sol-to-sol variations are present at the mid-latitude VL-2 site than at the low latitude VL-1 site. Later, in the early autumn at VL-2, Tillman (1977) and Tillman (1979), observed on the morning of sol 160, a clear example of a cold frontal passage. Extended analyses of time series, Zurek *et al.* (1991), lead to the conclusion that high and low pressure systems, similar to terrestrial ones, pass north of the VL-2 site roughly every 3.3 sols for approximately 100 sols. It also was suggested that the systems are often more strongly periodic than those on earth, and sometime resemble the flow regimes of laboratory rotating dishpan experiments (Tillman, 1977). Extensive descriptions of the Martian atmosphere can be found in the Zurek *et al.* (1991).

The meteorological context of these analyses can best be illustrated with the aid of Figure 1 showing the major characteristics over the first 669 sols of the mission, and the seasonal index, L_S, is given for each of the analyzed sols in Table 3. The first sol, 30, is in late summer before the beginning of significant baroclinic activity later in autumn, the sol 447 and 448 pair are during early spring after the 1977 B great dust storm (Tillman, 1988), while the last is during late spring, still a period of moderately low baroclinic activity.

3 Spectrum analysis

The selection, editing and spectral analysis techniques are described in this section as well as the method for transforming the measured variables into the coordinate system normally used in turbulence theory. This program was undertaken to develop comprehensive spectral modeling techniques and use them to determine atmospheric surface layer parameters for a few selected sols. Only measurements from VL-2 are used for this analysis. VL-1 had a partial failure of the wind system, beginning on sol 44, and a second one on sol 376 described by Murphy *et al.* (1991), and Chamberlain *et al.* (1976). Software subsequently has been developed that can partially compensate for these failures but its adequacy, range of applicability and accuracy have yet to be appropriately tested.

Limitations in the telemetry of data from Mars, controlled the sampling scenario for the two landers. The nominal strategy was to acquire about 2,200 measure-

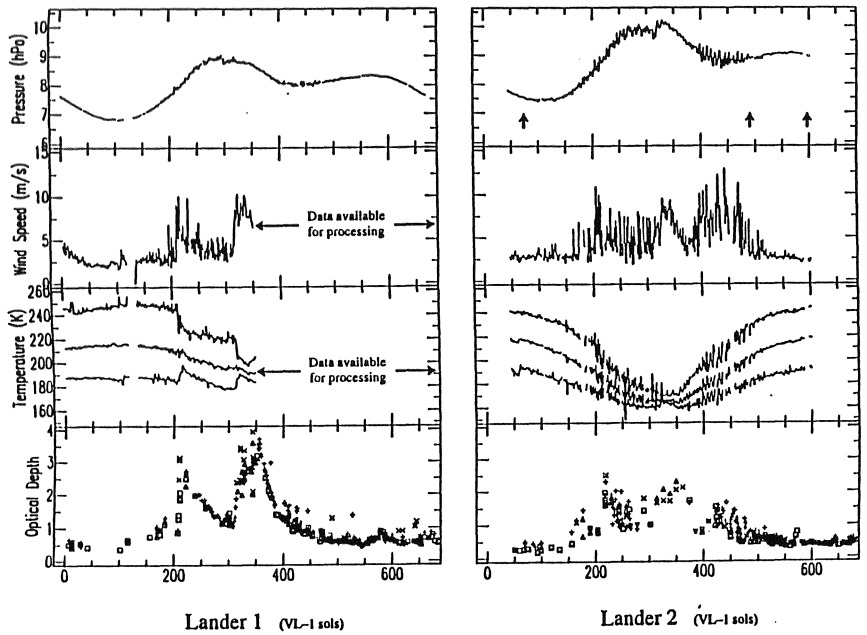

Figure 1. Pressure, temperature, wind speed and optical depth for the first 669 sols at Landers 1 and 2. Sol averages, top to bottom: Pressure – mean; temperature – minimum, mean and maximum; wind speed – mean; and optical depth – (from Colburn et al., *1989). Optical depth symbols indicating: AM; lower bound* × *, nominal* + *, upper bound* ∗ *, and PM; lower bound* □ *, nominal* △ *, and upper bound* ▽ *values respectively, Tillman, Murphy and Johnson, private communication 1991.*

ments/sol, sampling faster during day than night: the typical fast daytime interval was about 8 seconds. For the highest frequency acquisition scenarios, the meteorology experiment acquired part of the imaging and seismology data budgets on a very few selected sols, collecting up to 7,000 measurements/sol, using sampling intervals down to 1.2 seconds for a one hour period. These fast sampling periods were generally surrounded by 4.0 second sampling and were shifted throughout the sol to characterize the spectrum of the surface layer turbulence. At other times, they were concentrated during the daytime to better define daytime convective processes.

The calculation of spectra, and using their properties to infer that the results represent one element of an ensemble of a random processes, assumes that the process is stationary throughout the analysis interval. This is in conflict with the basic diurnal variability of the atmospheric surface layer, and the analysis of a portion of a diurnal cycle requires several cycles of low frequency processes, such as cellular or longitudinal convective elements or gravity waves to produce reasonable low frequency estimates. Stringent stationarity requirements are rarely met in any analysis of the unstable atmospheric boundary layer and these are no exceptions. Furthermore, the segments available for analysis were constrained by spacecraft operational decisions, are not optimum, and tradeoffs, such as having to vary the sampling rate during the sol due to data limitations, were made. For example, sol 554 is not very stationary, compared to the others, but it is used to illustrate the results of fast, daytime sampling during light wind conditions. Generally, these sols should represent the processes and season during which they were acquired.

3.1 Selection of spectra

In order to be sure that the spectra properly represent the turbulent boundary layer velocity, analyses were made for selected sols for which:

1. The direction of the wind is generally outside the range of lander interference, LI (i.e. wind from 126 to 212 degrees, where the lander body is upstream of the sensor array).
2. The sampling interval is constant during the entire duration of the sample.
3. The time series contains no spikes
4. The sol has one or more periods where the sampling interval is less than 10 seconds and preferably 1.2 seconds, the shortest interval used, with a duration of at least 30 minutes to one hour.

Flow over and around the lander changes both the wind and temperature field. Wind errors, compared to free stream, of up to roughly 15% are encountered at the sensor location and temperature excesses of up to 10 K at near zero lowest wind speeds. The temperature increase is greatest for wind blowing over the Radioisotope Thermoelectric Generators, RTG's, and for the lowest ambient temperatures. Time series selected for analysis in this paper are shown in Table 3. Most segments have few or no points with lander interference, LI, except for sol 554, and otherwise fulfill the conditions described above.

The selected time series was linearly detrended i.e., the least-square line of the series was subtracted. Because the time series is finite, it is also important that it begin and end with a value close to zero: the end points are so chosen.

Table 3. The start and end times (in decimal hours) of the selected time series. In column 2, n *means night (i.e. stable cases), and* d *day (i.e. unstable cases),* Δt *is the sample interval in seconds. For the seasonal index,* L_S 90 = *summer,* 180 = *autumnal equinox,* 270 = *winter and* 360 *or* 0 = *spring. Data quality with respect to lander interference, "LI", is indicated.*

Sol	L_S	Segment	Start	End	Δ t	LI
30	132.1	n1	19.67	20.89	64	OK
		n3	4.85	5.80	8	OK
447	15.5	d1	10.99	12.00	4.8	OK
		n1	0.67	1.63	15.8	OK
		n2	1.73	2.69	15.8	OK
448	16.0	d1	11.01	11.99	4.8	3 points
		d2	12.02	12.99	4.8	OK
		d3	14.02	15.00	4.8	OK
		n1	21.07	22.03	15.8	OK
		n2	22.13	23.10	15.8	OK
		n3	23.19	24.16	15.8	OK
554	65.1	d1	12.06	13.06	1.2	50%
		d2	13.06	14.06	1.2	50%

3.2 Transformation of the measured values

In turbulence theory the wind is considered as consisting of a mean and a fluctuating part. The x-axis is always taken along the direction of the mean wind. Since the Lander measures the wind speed and direction, it is necessary to transform

the velocity vectors into a coordinate system, where the x-axis is taken along the mean direction of the wind. The new coordinates (x',y') is given by the old (x,y) by the expression

$$x' = x\cos\phi + y\sin\phi \tag{1}$$

$$y' = y\cos\phi - x\sin\phi \tag{2}$$

where ϕ is the angle between the original x-axis and the mean wind vector.

3.3 Aliasing and filtering

Aliasing produces erroneous spectral estimates to the extent that energy exists at frequencies higher than the highest resolvable frequency, the Nyquist frequency, $n_N = 1/2\triangle t$, where $\triangle t$ is the sampling interval. Energy at frequencies above n_N, is folded into the frequencies between zero and the Nyquist frequency. Since the sampling rates are generally very slow, Table 3, the effect of aliasing is quite severe and must be incorporated into either the models or corrected for in the estimated spectrum: correcting the model spectrum has been chosen for this analysis. The effect of aliasing, if the real spectrum is known, is given by

$$S_m(n) = \sum_{k=-\infty}^{\infty} S_u(n + kn_s)\ n = 0 \ldots n_N \tag{3}$$

where S_m is the measured spectrum, S_u the real unaliased model spectrum, $n_s = 1/\triangle t$ is the sampling frequency, and $\triangle t$ the sample interval. In practice the summation converges, so that it can be truncated over a finite interval (e.g., -100 $< k <$ 100).

The effect of aliasing, depicted above, is somewhat limited by the filtering due to the response time of the sensors used. The temperature sensors are 75μ diameter chromel constantan thermocouples, Chamberlain *et al.* (1976). The worst case time constant at a pressure of 2.1 millibars and a wind speed of 2 m/s is on the order of 1.8 seconds (Davey *et al.*, 1973). Since the pressure is higher and the speed generally larger, more appropriate values range from 1.3 to 0.98 seconds or less: for these calculations, the time constant for the temperature sensor was chosen to be 1.0 seconds. The wind system consists of two different sensors; 1), a pair of hot film anemometers, and 2), a wind direction ambiguity resolving quadrant sensor. The hot film time constants range from 0.043 to the order of 0.2 seconds. The quadrant sensor uses the same size thermocouples as the temperature sensor and its worst case time constant is separately specified as 1.24 seconds. Hot film and quadrant sensor are combined in a highly non–linear multi–dimensional optimization technique, and an approximate time constant of 0.2 seconds has been chosen to represent the wind system filtering. Information necessary to better estimate the variations of the time constants with wind speed and direction is not readily available. With these choices, it is assumed that the temperature and velocity signal filtering can be approximated by first order, low pass filters with 3 db frequencies of 0.1 and 0.8 Hz respectively.

4 Distortion of the flow by the lander

Due to the small distance of the Meteorology Sensor Assembly, MSA, from the lander, the lander influenced the wind speed and temperature measurements. Wind

tunnel measurements carried out in the NASA Langley transonics dynamic tunnel prior to the launch, showed that, in the area outside the Lander Interference region, "LI", the wind reduction was in the range of 90 – 99%, see Chamberlain *et al.* (1976) and Greene *et al.* (1972). Prior to the design and placement of the supporting boom and MSA on the lander, wind tunnel studies were made to determine the best placement of the MSA, within spacecraft design constraints: this was slightly in front of footpad #2 (Chamberlain *et al.*, 1976). When the sensor assembly was within a 120° cone downwind of the lander, the errors were significant, while outside this region, they were minor. (In the wake of the lander, temperatures are increased by the thermal plume of the lander, especially due to heating from the Radioisotope Thermoelectric Generators, RTG's.) The wind speed errors for this configuration are estimated from wind tunnel measurements and by potential flow calculations. The accessible wind tunnel measurements are described by Greene *et al.* (1972) using a 0.45 scale model in the NASA Langley transonics dynamic tunnel. The tunnel has a working section diameter of greater than 6 metres, and wind speeds from about 10 *to* 150 ms^{-1}, and pressures near 10 millibars were used for these tests. Hot film anemometers were used in a survey mode to traverse the tunnel at scaled heights representing lander heights of 0.34 to 2.9, metres upstream and downstream of the lander. In many instances, transverses could not be made due to the presence of the lander or the communications antenna on top of the lander. These often precluded estimating wind errors at the MSA position, especially for serious lander interference conditions. Consequently, the 120° of azimuth which have severe lander interference are almost completely excluded from the high frequency analyses and most temperature estimates.

Outside of the severe LI azimuths, at heights of 1.02 metres, the worst LI wind speeds, relative to uncontaminated flow, for three antenna configurations range from 90% to 99% of the free stream values while at 1.69 metres the values are 95% to 99%. For these measurements, the MSA is at the right, upwind corner of the triangular lander. With the wind blowing parallel to the lander side and the MSA downwind of the lander, it is in the edge of the severe LI zone. Here the errors range between 5 and 20% at 1.02 metres height and $<$ 5% at 1.69 metres by interpolating measurements made upwind and downwind of the actual MSA position: measurements at the position were not available. The greatest measured errors occur in the wake of the lander with the antenna at the worst position, where the wind speed ranges from a low of 10% to a high of 110% of the free stream velocity. (In the tunnel tests, zones immediately downwind of the lander generally were not measured for safety.) The basic conclusion is that the errors are small outside the LI zone and almost always indicate a wind speed lower than free stream. Angle of attack errors for the same measurement suite, were a maximum of 20° at very rare points.

Other estimates of the effect of flow distortion were made by assuming potential flow around the lander. The first approximation is to assume that the surface follows the lander. This can be seen not to be completely true, since it is expected that the lander induces a squeezing of the streamlines. This effect can be investigated by assuming that the lander is a sphere that is partly submerged into the surface, see Figure 2, and then use the hydrodynamic theory developed for a sphere moving in an inviscid fluid with constant velocity, U. There are some assumptions that must be made, to use the theory developed. An obvious one is, that the lander can in fact be considered as a part of a sphere. Examination of the Lander, e.g. Chamberlain *et al.* (1976), shows that the space between the Lander and the surface is small, and has additional blockage due to the "bag-like" covers on the terminal descent rocket fuel cells hanging below the lander, therefore to a first approximation, flow below the lander is considered to be zero. A second assumption is that it is possible to use the theory developed for a sphere,

only for a part of a sphere. This is clearly an approximation, because some of the streamlines originate from below the surface, since the sphere is squeezing the streamlines. Another assumption is that the flow as inviscid. A final assumption is that the measured wind is horizontal, as would be the case in a neutral boundary layer. During very light winds, convective plumes, either due to atmospheric convection or the thermal plume from the RTG, will produce a vertical wind component which would generate velocity and angle errors: this effect should most noticeable below one to two ms^{-1}. At such times, the measured temperature may exceed the atmospheric temperature by up to 10 K.

The two desired parameters are:

1. The free stream height above the surface of particles passing the lander instruments.
2. The magnitude of the velocity, that would be measured if the flow was not disturbed by the lander, called the free stream velocity.

Using the stream function for a sphere, the free stream velocity, U, and the effective measurement height, z_{eff}, are given by (see Appendix A):

$$U = 0.87\,|\vec{v}| \tag{4}$$

$$z_{eff} = 0.93 \text{ m} \tag{5}$$

Since the potential flow results are based on the assumption that the sensors are directly upstream of the lander body, the correction will be smaller for wind coming from a more oblique angle. It is assumed that the potential flow wind speed, with its associated measuring height, is likely to be between the undisturbed values and those given by 4 and 5. To estimate the effect of this variation, all calculations have been carried out in two versions: one where the height is 0.93 m, with a velocity of 0.87 times the measured velocity and one with the height being 1.61 m and the measured velocity. The wind tunnel experiments were carried out using a model without the covers on the fuel cells and without the RTG covers, the latter resulting in the exposure of the aerodynamically very rough fins of the RTG. Unlike the potential flow calculations, the velocity is almost always smaller than free stream although the model is aerodynamically much rougher than the lander. The flow blockage by the fuel cell covers under the lander, and the smoothness of the actual lander, suggest that the flow on Mars should be closer to the potential flow calculations than would be indicated by the "rough model" measurements. It should be safe to conclude that the undisturbed wind speeds measured at the sensor height are bounded by those of the potential flow calculations and the wind tunnel model. The estimated wind speed errors from the flow calculations and from the wind tunnel measurements, do not appear to exceed ±15% in the 120° "no lander interference" region.

5 Derivation of L, u_* and H

It is necessary to scale the spectra to determine if they obey similarity theory which in turn requires calculation of the Monin-Obukhov length, L, the friction velocity, u_*, and the convective heat flux, H. Following the procedures of Sutton *et al.* (1978) these can be estimated from the values of: the mean velocity, U, at height z, the atmospheric temperature at height z, T_{atm}, and the temperature at the surface, T_{surf}, where z is the effective instrument height (0.93 m $\leq z <$ 1.61 m). The first, and most significant problem, is that the lander measurements were only made at one height, z, and the surface temperature must be modeled. Sutton *et al.*

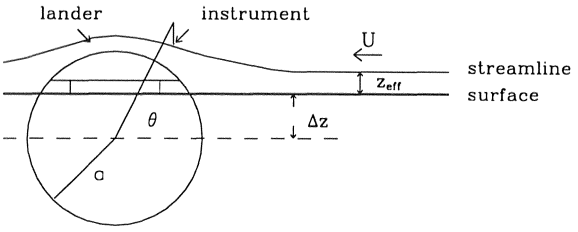

Figure 2. The lander and the circumscribed sphere. z_{eff} is the effective height of the air parcels arriving at the sensor and Δz is the displacement of the centre below the surface of the sphere circumscribing the lander. a is the radius of this sphere. r is the distance from the centre of the sphere to the instrument. θ is the angle between horizontal and the line connecting the centre of the sphere and the instrument. U is the free-stream velocity.

(1978) calculated surface temperatures with a model assuming uniform thermal inertia and albedo values, determined by Kieffer (1976), and a solar declination angle appropriate for the center of their analysis period and point out that "Some significant departures from the homogeneous surface model have been found in the latitude belt of the VL-2 site. At these locations, ground temperature falls below that predicted by the homogeneous surface model between 1400 and 1900 LLT, with a discrepancy of as much as 10° C."

The values of surface temperature used here are produced by the mission operations software, SANMET, Appendix B. Similar to Sutton *et al.* (1978) the bulk Richardson number, Ri_B, is[3]

$$\mathrm{Ri}_B = \frac{gz\Delta\theta}{U^2 T} \tag{6}$$

where g is Martian surface gravity (=3.72 m s^{-2}), $\Delta\theta$ the difference between the potential temperature at instrument height and at the surface[4], u is the wind speed, T is the mean value of the surface temperature and the atmospheric temperature. From the bulk Richardson number they calculated the Monin-Obukhov length

$$L = -\frac{\rho c_p T u_*^3}{kgH} \tag{7}$$

where c_p is the specific heat at constant pressure, ρ the atmospheric density, k (=0.4) Von Kármán constant, and H the convective heat flux (positive upwards). (See Appendix C for c_p and ρ values.)

The relation between L and Ri_B is found by using similarity theory which states that

$$\frac{du}{dz} = \frac{u_*}{kz}\phi_m(\zeta) \tag{8}$$

and

$$\frac{d\theta}{dz} = \frac{H}{\rho c_p k u_* z}\phi_h(\zeta) \tag{9}$$

where ϕ_m and ϕ_h are universal functions of $\zeta = z/L$, a dimensionless height. The behavior of these two functions is empirically known from experiments in the terrestrial boundary layer, cf. Businger *et al.* (1971), Dyer (1974). Integrating

[3]This method was also used by Sutton *et al.* 1978, although without correction for flow distortion. They used the actual height of the instruments, z = 1.61 m.

[4]Since the height difference is only 1.6 metres maximum, ΔT is used instead of $\Delta\theta$.

Eqs 8 and 9 from z_0 and z_{0T} respectively, to z, and substituting the results into Equation 6 yields

$$Ri_B = \frac{\zeta \int_{\zeta_{0T}}^{\zeta} \zeta^{-1}\phi_h(\zeta)d\zeta}{\left(\int_{\zeta_0}^{\zeta} \zeta^{-1}\phi_m(\zeta)d\zeta\right)^2} = f(z, z_0, z_{0T}, L) \tag{10}$$

where $\zeta_0 = z_0/L$, $\zeta_{0T} = z_{0T}/L$. In Equation 10, z_0 is the surface roughness, while $z_{0T} < z_0$ is the corresponding scale height for the temperature profile: it is assumed that the surface temperature estimated by SANMET corresponds to the temperature at z_{0T}. (See Appendix D for estimates of z_{0T}.) In the present analysis, we use three z_0 values, 3.0, 1.0 and 0.3 cm which, with assumptions, yield z_{0T} around 0.1 cm with some variation with u_*: we have neglected this variability, which is less than 40% and simply assumed $z_{0T} = 0.1$ cm for all z_0-values tested. Sutton *et al.* (1978) assume $z_{0T} = z_0$, and check their results against another model where the turbulent layers considered here are separated from the surface by a molecular conduction layer. They find little difference between L and u_* from their two models, while differences up to 20 to 30% are found for the heat flux.

For the universal behavior of ϕ_h and ϕ_m we have used the expressions of Dyer (1974), as opposed to Sutton *et al.* (1978) who used Businger *et al.* (1971),

$$\phi_m = \begin{cases} 1 + 5\zeta & \zeta > 0 \\ (1 - 16\zeta)^{-1/4} & \zeta < 0 \end{cases}$$

$$\phi_h = \begin{cases} 1 + 5\zeta & \zeta > 0 \\ (1 - 16\zeta)^{-1/2} & \zeta < 0 \end{cases}$$

When z, z_0, and z_{0T} are fixed the right side of Equation 10 is a monotonic function of L, except for extremely stable cases. An example of the results of this calculation is seen in Figure 3. The behavior of L, as a function of time on Mars, is seen to be hyperbolic like that on Earth. The order of magnitude is seen to be like that found by Sutton *et al.* (1978).

The friction velocity and the convective heat flux is given by integrating Eqs 8 and 9, respectively. This yields

$$u_* = C_d(\zeta, \zeta_0, \zeta_{0T})u$$

$$H = -\rho c_p u_* C_h(\zeta, \zeta_0, \zeta_{0T})\theta$$

where the drag coefficient C_d is given by

$$C_d = k\left(\int_{\zeta_0}^{\zeta} \zeta^{-1}\phi_m(\zeta)d\zeta\right)^{-1}$$

and the heat transfer coefficient C_h by

$$C_h = k\left(\int_{\zeta_{0T}}^{\zeta} \zeta^{-1}\phi_h(\zeta)d\zeta\right)^{-1}$$

6 The height of the convective boundary layer

In order to find the right spectral model for the unstable spectra it is necessary to know or estimate the height of the lowest inversion. A model based on the first law of thermodynamics is used. Assuming a column of air (see Figure 4), of height h, and that heat is added at the top and at the bottom, given by Q_i and

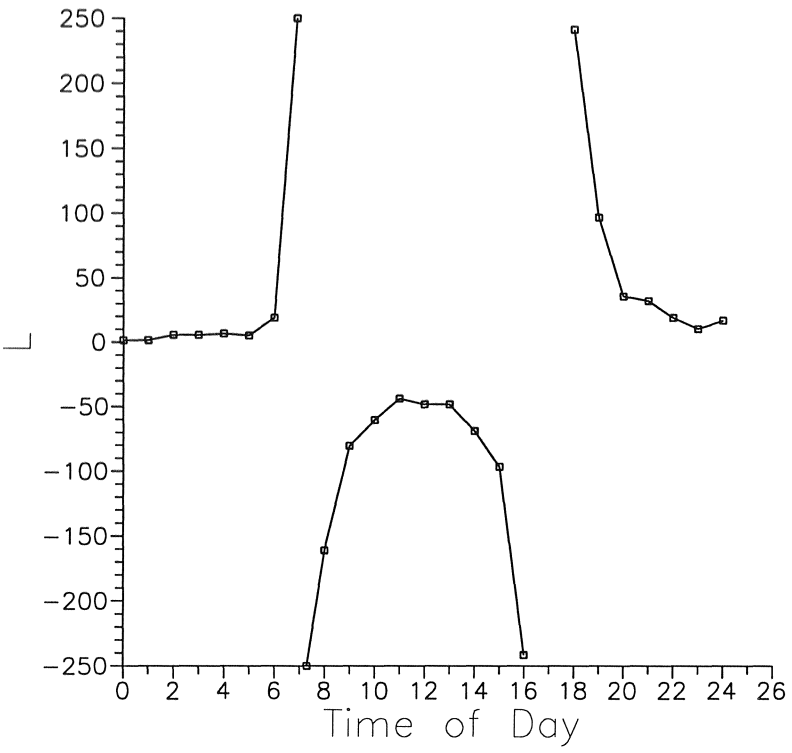

Figure 3. Plot of L from sol 448.

Q_0, respectively, the first law of thermodynamics gives the rate of change of the average potential temperature of the boundary layer column, θ_m, as

$$\frac{d\theta_m}{dt} = \frac{Q_0 - Q_i}{h}$$

Applying the chain rule on the left-hand side with respect to h, yields

$$\frac{d\theta_m}{dh}\frac{dh}{dt} = \frac{Q_0 - Q_i}{h}$$

where the first term now represents the change of the temperature of the boundary layer when the height of the boundary layer changes, and the second the change of the height with time. Using the parameterization of Q_i of Deardorff (1979), $Q_i = -0.2Q_0$, and replacing $d\theta_m/dh$ by the lapse rate, γ_h, results in

$$h\frac{dh}{dt} = \frac{1.2Q_0}{\gamma_h}$$

Integrating this from $t' = t_0$ to $t' = t$ yields

$$h = \left(\gamma_h^{-1}\int_{t_0}^{t} 2 \cdot 1.2Q_0 dt' + h^2(t_0)\right)^{\frac{1}{2}} \tag{11}$$

t_0 is the time when the surface starts to be warmer than the atmosphere, i.e. when Q_0 starts to be positive. As previously described, $Q_0(t)$ is derived from SANMET inferred surface temperatures and temperature and wind speed calculated from the VMIS. For these calculations, γ_h is taken from the entry data of Seiff, and varies with location and time of day as shown by Lindal et al.: other γ_h initial profiles would produce different depths[5]. $h(t_0)$ is zero, as morning convection starts to "raise" the inversion from the surface.

[5]It is found, however, that the calculation of h is not very sensitive to the expected variations of γ_h

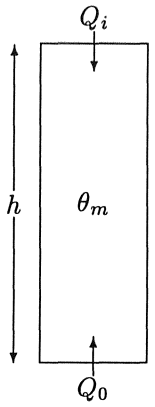

Figure 4. Definition sketch of an air column

Daytime boundary layer depths for selected sols are presented in Table 4, and the development of the height during the day is given in Appendix E. All combinations of 3 values of z_0, 0.3, 1.0, and 3.0 cm, and the two effective instrument heights, 0.93 and 1.61 m, were used but only the values for 0.93 m are presented[6]. Heights of 3.5 to 9.1 km are obtained, and calculations by Haberle in Zurek *et al.* (1991) support similar daytime depths and Sutton *et al.* (1978) suggest early summer, mid–afternoon depths on the order of 5 km. Tillman (1977) estimates heights of 2.5 km from orbital images at 12° S at noon, and from lander wind measurements, suggests that daytime convective scales range between 1 and 10 km. Comparing the Martian values to typical values on Earth (1000 m), the boundary layer on Mars is deeper than the typical terrestrial boundary layer, excluding latent heat dominated convection.

Due to the lower density on Mars, as contrasted with Earth, the surface temperature is mainly determined by radiative balance and is less dependent on wind speed. Conversely, given the same radiative, surface roughness, thermal inertia, albedo and topographic conditions, the surface temperature does not change much with wind speed and, therefore, the heat flux, and related variables such as z_i are essentially determined by wind speed. Selecting a z_0 of 1.0 cm from Table 4, sol 448 has a depth of 7.0 km as contrasted with 5.3 km on sol 447. This is essentially all due to the larger wind speed which causes the heat flux of sol 448 to be higher by a factor of 2. $(T_{atm} - T_{surf})$ is essentially the same for sols 447 and 448 since the optical depths are the same. [7]

7 The models

The description of the models is covered in two sections, one covering the stable cases, and the other the unstable cases. In some instances, generally accepted models do not exist.

[6]These estimates are to be considered an approximation since radiative heating and cooling are not incorporated.

[7]Since the time of the maximum wind speed does not generally correspond to that of the maximum temperature gradient, the heat fluxes are not exactly proportional to the wind speed.

Table 4. The height of the boundary layer in km, from Equation 11, and other parameters, for selected sols. The values are for the 0.93 metre effective measuring height, and differ slightly from those for the 1.61 metre height. $\overline{U}$, H, T_{surf}, and $(T_{atm} - T_{surf})$ are the maximum values during the sol: T_{sky}, T_{surf} and τ are from VCF SANMET.

Sol	447	448	554
	Depth in km		
h ($z_0 = 0.3cm$)	4.2	5.5	3.6
h ($z_0 = 1.0cm$)	5.3	7.0	4.5
h ($z_0 = 3.0cm$)	7.0	9.2	5.8
Maximum during sol, except τ			
u_*	0.42	0.72	0.27
$\overline{U}(ms^{-1})$	4.60	8.10	3.40
H (Wm^{-2})	13.50	25.00	10.70
$(T_{atm} - T_{surf})$	26.60	27.20	26.80
T_{sky}	190.00	190.00	
T_{surf}	246.35	246.40	261.71
τ	0.499	0.504	

7.1 Stable cases

Model of stable horizontal velocity spectra

The models for stable horizontal velocity spectra were developed by Olesen *et al.* (1984), and further substantiated in Larsen et al. (1985), such that they fulfill all the following conditions

- The inertial subrange should be consistent with Kolmogoroff's law

  $$E(\kappa) = \alpha_1 \epsilon^{2/3} \kappa^{-5/3}$$

  where E is the energy, κ the wave number, α_1 a constant and ϵ the dissipation rate.

- The spectral maximum of the measurements should coincide with the maximum of the model, both with regard to frequency and amplitude.

- Finally, the integral scale of the measured spectrum should equal that of the model.

Model spectra that fulfill all of the above criteria are of the form

$$\frac{nS(n)}{u_*^2} = \frac{Af^\gamma}{(1 + Bf^\alpha)^\beta}.$$

Data from the Kansas and the Minnesota experiments, led Olesen *et al.* (1984), to conclude that the best models for the horizontal spectra are

$$\frac{nS_u(n)}{u_*^2} = \frac{79x}{1 + 263(x)^{5/3}} \left(\frac{\phi_\epsilon}{\phi_m}\right)^{2/3} \quad \text{for } u$$

and

$$\frac{nS_v(n)}{u_*^2} = \frac{13x}{1 + 32(x)^{5/3}} \left(\frac{\phi_\epsilon}{\phi_m}\right)^{2/3} \quad \text{for } v$$

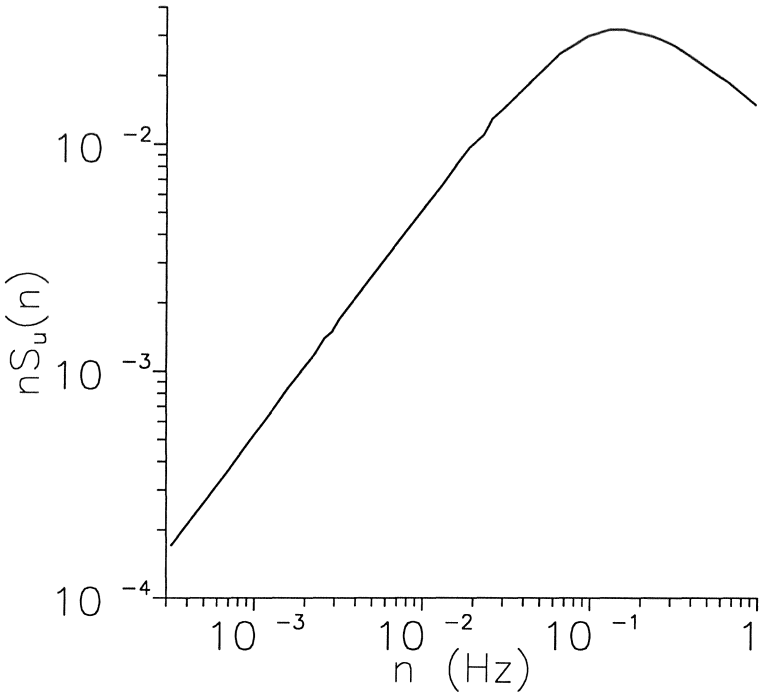

Figure 5. The model for stable velocity spectra. The model shown is for the u-component.

where S is the power spectrum, n the frequency, u_* the frictional velocity, $x = f/\phi_m$, $f = nz/U$, the reduced frequency, and $\phi_\epsilon^{2/3} = 1 + 2.5(z/L)^{0.6}$. A plot of this model is shown in Figure 5.

If gravity waves are present, the measured low frequency portion of the spectrum can diverge from the model (cf. Olesen *et al.*, 1984). The divergence is of the form of a line with slope -3, remembering that on the $(n,nS(n))$-plots used in this paper the slope will seem to be -2. The line is given by

$$\frac{nS_\alpha(n)}{u_*^2} = \gamma_\alpha \frac{z}{L}\phi_h f^{-2} \tag{12}$$

The frequency, f_{gap}, up to which the n^{-3} behavior is dominating has been shown by Olesen *et al.* (1984) to be

$$f_{gap} = \left(2\frac{\gamma_\alpha}{A_\alpha}\frac{z}{L}\phi_h\phi_m^{5/3}\phi_\epsilon^{-2/3}\right)^{1/3}$$

where $\alpha = u, v$, and $\gamma_u = \gamma_v = 4 \cdot 10^{-6}$, $A_u = 79$ and $A_v = 13$.

Model of stable temperature spectra

The stable temperature spectral model developed by Kaimal *et al.* (1976), given by

$$\frac{nS_\theta(n)}{\bar{\theta^2}} = \frac{0.16(f/f_0)}{1 + 0.16(f/f_0)^{5/3}}$$

is used, where $\bar{\theta^2}$ is the variance of θ, and $f = nz/U$ the reduced frequency, and f_0 can be approximated by z/L. A plot of the temperature spectral model is shown in Figure 6.

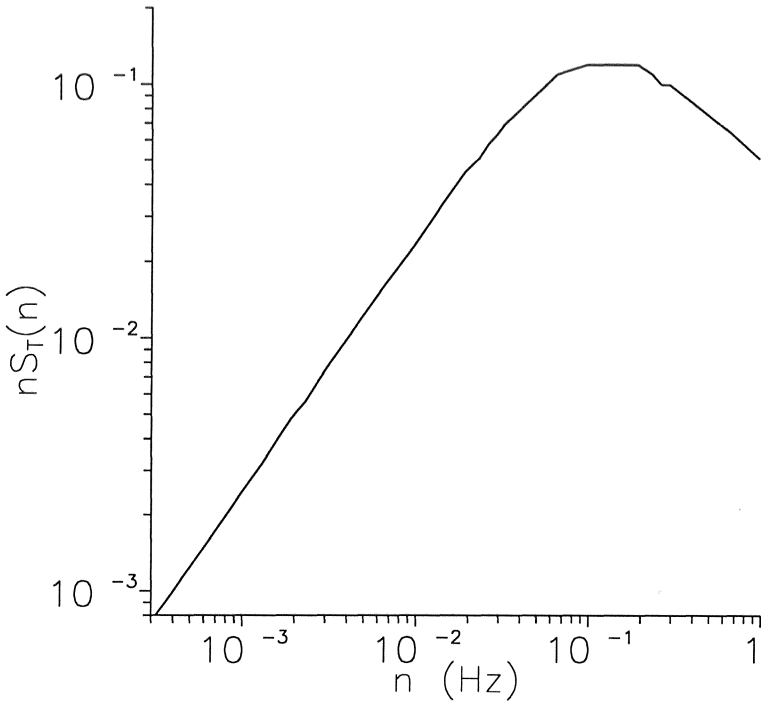

Figure 6. The model for stable temperature spectra.

7.2 Unstable cases

Model of unstable horizontal velocity spectra

The model developed by Højstrup (1982) consists of two parts: one part buoyancy-produced and one shear-produced. It is assumed that the two models do not interact, i.e. they have their own separate spectral domains. This is true only close to the ground, but it seems to be a good approximation in general. The buoyancy-produced part of the model scales with the height of the lowest inversion, z_i, and the shear-produced part with the instrument height. The resulting models of the components of the horizontal spectra are, respectively

$$\frac{nS_u}{u_*^2} = \frac{0.5f_i}{1+2.2f_i^{5/3}}\left(\frac{z_i}{-L}\right)^{2/3} + \frac{105f_{ru}}{(1+33f_{ru})^{5/3}}\frac{(1-z/z_i)^2}{(1+15z/z_i)^{2/3}}, \text{ for } u$$

$$\frac{nS_v}{u_*^2} = \frac{0.95f_i}{(1+2f_i)^{5/3}}\left(\frac{z_i}{-L}\right)^{2/3} + \frac{17f_{rv}}{(1+9.5f_{rv})^{5/3}}\frac{(1-z/z_i)^2}{(1+2.8z/z_i)^{2/3}}, \text{ for } v$$

where

$$f_i = nz_i/U$$

$$f_{ru} = f/(1+15z/z_i)$$

and

$$f_{rv} = f/(1+2.8z/z_i)$$

a plot of this model is shown in Figure 7.

The model holds well for measurements at 10 m and above. For lower levels, there is a "squeezing" of the length scale, z_i, which has been modeled by a simple exponential form

$$z_{i,new} = (1-\exp(-z \qquad _i. \qquad /7))\cdot z \tag{13}$$

This has been tested on Earth down to 3 m, Højstrup *et al.* (1990) and is applied down to 0.93m for these models. Although it produces internally consistent results, its accuracy should be verified.

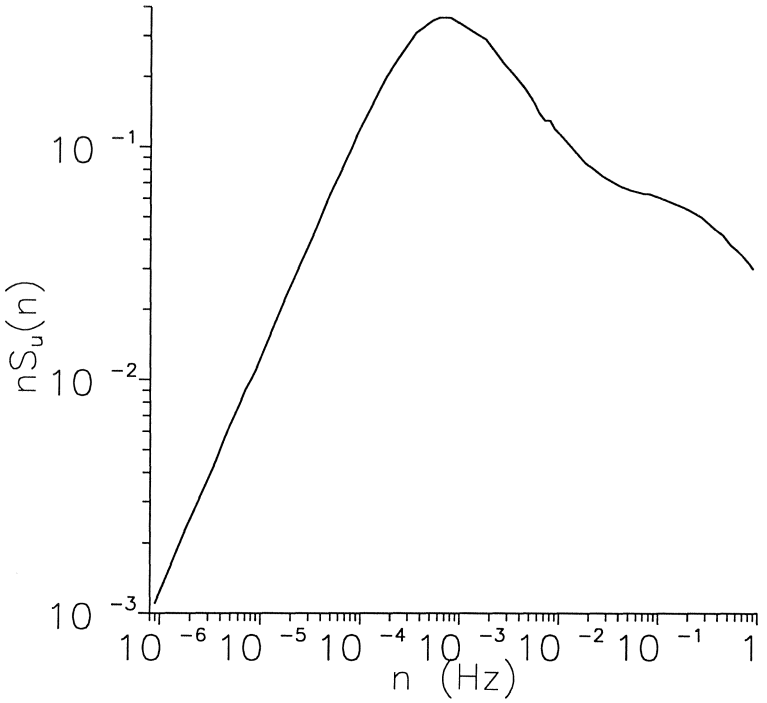

Figure 7. The model for the u-component of the unstable velocity spectra. Note the two 'bumps', due to the fact that the model is the sum of two (sub-)models, with different spectral domains.

Model of unstable temperature spectra

Analytical models for unstable temperature spectra do not exist but Kaimal *et al.* (1976) have suggested idealized curves for these cases. Since unstable temperature data are not presented for reasons described later, the "idealized" curves are omitted.

Kolmorogov scale

At wave numbers above the Kolmogorov scale of viscous dissipation, η, the spectral energy density decreases more rapidly with increasing wave number than in the inertial sub-range, cf. Lumley and Panofsky (1964). The Kolmogorov scale is given by

$$\eta = (\nu^3/\varepsilon)^{1/4}. \tag{14}$$

and is larger in the Martian atmosphere, than on Earth due to the larger kinematic viscosity Sutton *et al.* (1978).

The dissipation cut-off can be written in terms of the reduced frequency, f_ε, (cf Larsen *et al*, 1985)

$$f_\varepsilon = z/2\pi(10\eta) = \frac{\kappa^{-1/4}}{20\pi}\varphi_\varepsilon^{1/4}(z/L)\left(\frac{zu_*}{\nu}\right)^{3/4} \sim 0.7 \tag{15}$$

using as typical values for the data considered $\varphi_\varepsilon \sim 1$, $z = 1$ m, $u_* = 0.2$ m/s, $\kappa \approx 10^{-3}$m^2/s and $\nu \approx 10^{-3}$ m^2/s.[8] The corresponding frequency cutoff [Hz] is found from $n_\varepsilon = f_\varepsilon \overline{u}/z$, and from the parameters characterizing each run in Appendix A, it can be shown that n_ε for some of the runs is lower than the instrumental low pass frequencies previously discussed. In practice, the dissipation cutoff is introduced

[8] κ and ν relations were adapted from linear fit to temperature dependent data which warrant a quadratic for accuracy: however, for this approximate calculation approximate values are used.

by multiplying the forms above by $\exp(-n/n_\varepsilon)$, with n_ε found from the equation above for each run: in the above discussions, no distinction is made between the Kolmorogov scales for temperature and velocity. A consequence of this larger Martian Kolmorogov scale than on Earth, is that the inertial subrange is virtually absent from the turbulence in the Martian atmospheric surface boundary layer. This can be seen by considering the peak for the power spectrum of the vertical velocity spectrum. This peak is found for $f_{peak} \approx 0.5$. According to discussions in Kaimal *et al.*, 1972 and Larsen *et al.*, 1985 the lower boundary for the inertial subrange is to be found around 5-10 times f_{peak}. Comparison with Equation 15 therefore shows that the dissipation range starts before the inertial range can be established.

8 Comparison of measured and model spectra

After incorporating the above corrections into the model, the corrected model spectra are compared with the measured spectra, first for the stable cases and then for the unstable.

8.1 Stable cases

Velocities

With the aliasing, instrumental, and Kolmorogov scaling corrections to the models, there generally is good agreement between the measured and the modeled spectra. A few examples are shown here and when the measured spectra diverge from the model, they generally follow the expected n^{-3} gravity wave behavior. Calculations of f_{gap} produces good agreement between data and theory. Estimating the coefficient γ_α, for the u-spectrum, gives $\gamma_u = 1.7 \cdot 10^{-7}$, compared to $4 \cdot 10^{-6}$ that Olesen et al. (1984) found. On Earth, they found that the predicted value is smaller than the observed value. Using the γ_α found by Olesen et al., the predicted value is higher than the observed in all cases. An example is given in Figure 8. There are some cases where f_{gap} is within the spectral band of the measured spectrum, but where the n^{-3} behavior is absent. This can be explained by the fact that even though there is the possibility of gravity waves, they do not necessarily exist.

Temperatures

Comparing the the model spectrum with the measured spectrum for stable, nighttime conditions, Figure 9, the agreement is fairly good in the low frequency portion of the spectrum while the spectral density is low for the highest measured decade. The latter is probably is due to the low level of variability during stable conditions coupled with the poor, $\approx 0.8\ K$, resolution of the temperature measuring system.

8.2 Unstable

Velocities

Using the largest value of the height of the boundary layer found for sol 447 d1 in the unstable, horizontal spectral model, good agreement is found between the observed and the model spectrum, see Figs. 10 and 11. On sol 554, see Figure 12,

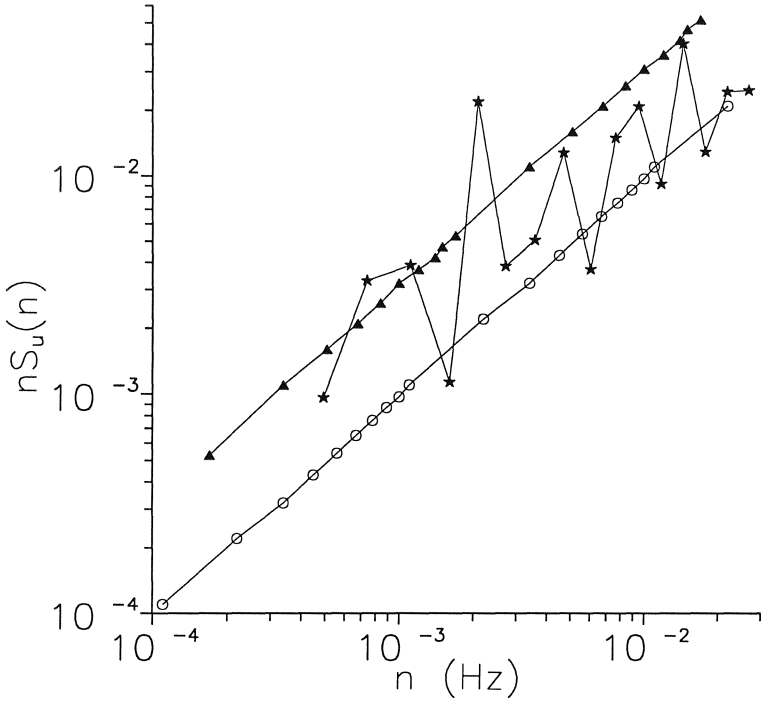

Figure 8. A stable u-spectrum, from sol 448, n2. ⋆ − ⋆ is the measured spectrum, solid triangles are the aliased modeled spectrum with z_{eff} = 0.93 m and z_0 = 3.0 cm, ∘ − ∘ is the aliased modeled spectrum with z_{eff} = 1.61 m and z_0 = 0.3 cm, the straight dashed line represents the model taking aliasing into account, and the bell-shaped dashed line is the unaliased model.

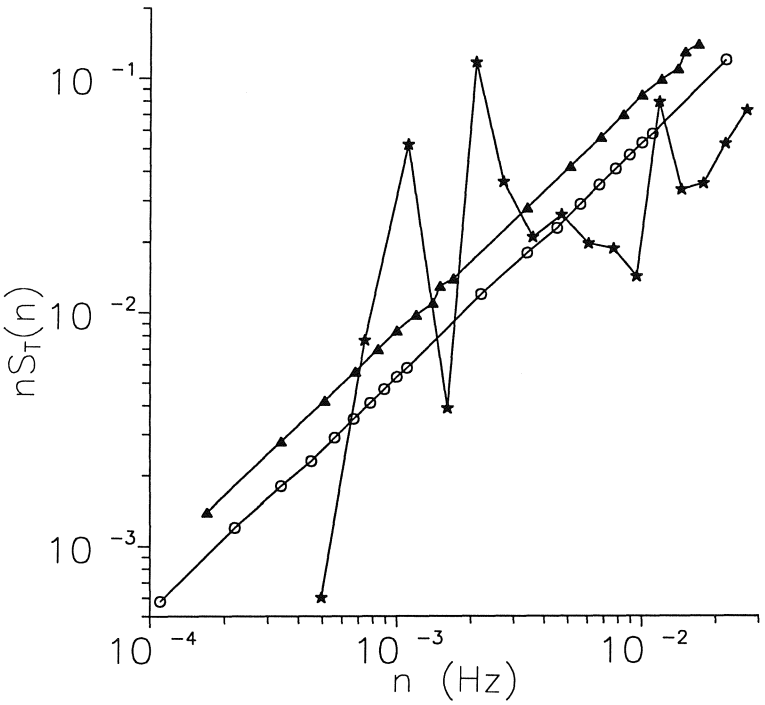

Figure 9. A stable temperature spectrum for sol 448, n2. ⋆ − ⋆ is the measured spectrum, solid triangles are the aliased modeled spectrum with z_{eff} = 0.93 m and z_0 = 3.0 cm, ∘ − ∘ is the aliased modeled spectrum with z_{eff} = 1.61 m and z_0 = 0.3 cm, the straight dashed line model only incorporates aliasing.

the scan rate is 1.2 s – as contrasted with 4.8 s on 447 d1 – and the agreement between the high-frequency part of the spectral density of the data and the model is also very good.

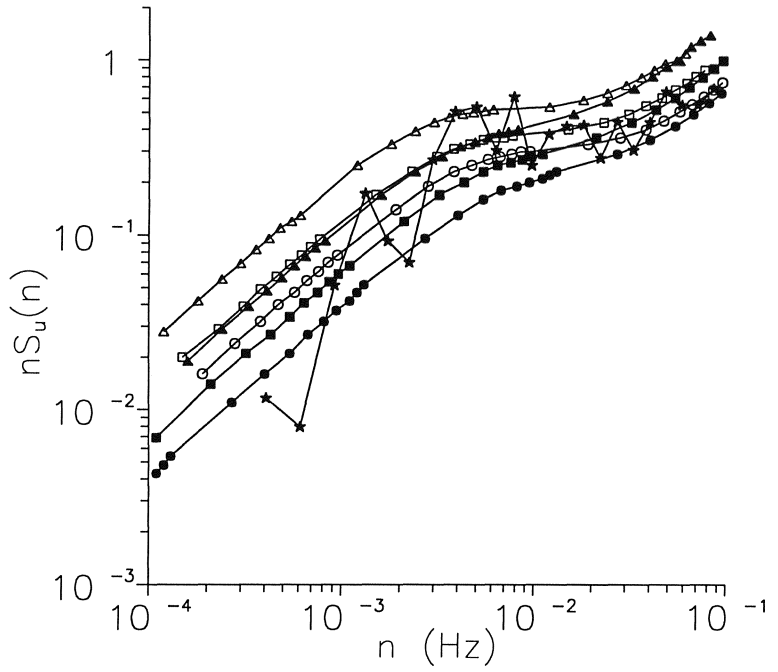

Figure 10. Model and measured spectrum of the u-component of the velocity in the unstable case, for sol 448, d2, sample interval =4.8 s, z_i= 4,394 m. Corrected, model spectra are calculated for the three z_0's and two effective measuring heights. ⋆–⋆ is the measured spectrum. For the model spectra, the symbols for the z_0's are: ○ 0.3 cm, □ 1.0 cm, △ 3.0 cm. Solid symbols indicate a height, z, of 0.93 m while open symbols indicate a height of 1.61 m.

Temperatures

The temperature data are not presented for two reasons. First, there is no "model" unstable temperature spectrum and second, there is excessive noise in some of the unstable temperature measurements. The temperature system's previously mentioned low resolution, coupled with rapid changes in the mean temperature when the MSA heater is cycling at temperatures below 234°K, introduce noise at high frequencies: this noise becomes worse as the sampling interval decreases. At a 1.2 second sampling interval, it has been analyzed and modeled and the increase in spectral density above 0.02 Hz for a midday segment of sol 448, (not shown), with a 4.8 second sampling interval, may be mostly due to this effect. Most of the high frequency noise at fast sampling rates is confined to quite narrow spectral lines whose frequency can be predicted. Therefore, it can be modeled and predicted and experiments have been carried out. [9] Midday measurements during warmer seasons are far less contaminated, as the heater is not in operation above temperatures greater than 234° K.

[9] Although this can not be done with the current resources, it can be developed for future analyses.

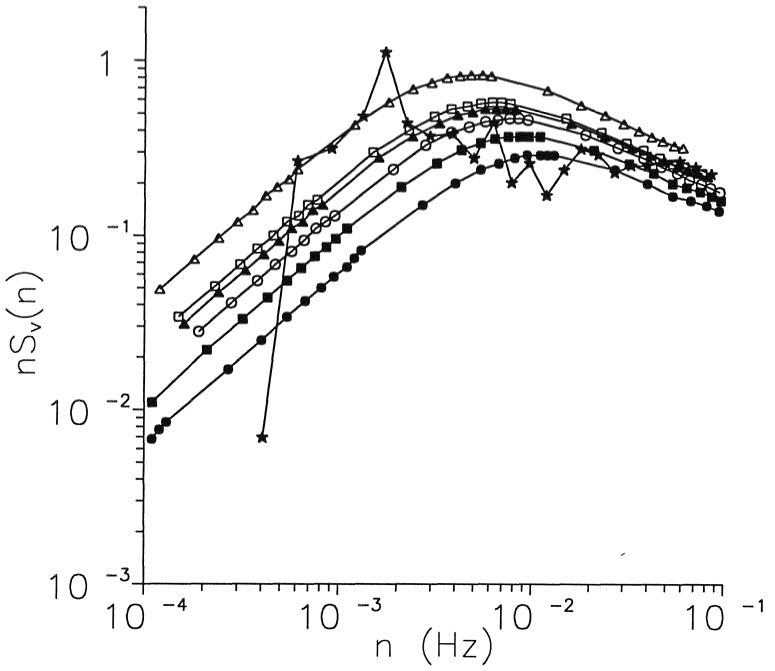

Figure 11. Spectrum of the v-component of the velocity in the unstable case, from sol 448, d2, sample interval = 4.8 s, z_i=4,394 m. Corrected, model spectra are calculated for the three z_0's and two effective measuring heights. ⋆–⋆ is the measured spectrum. For the model spectra, the symbols are the same as for the u component above.

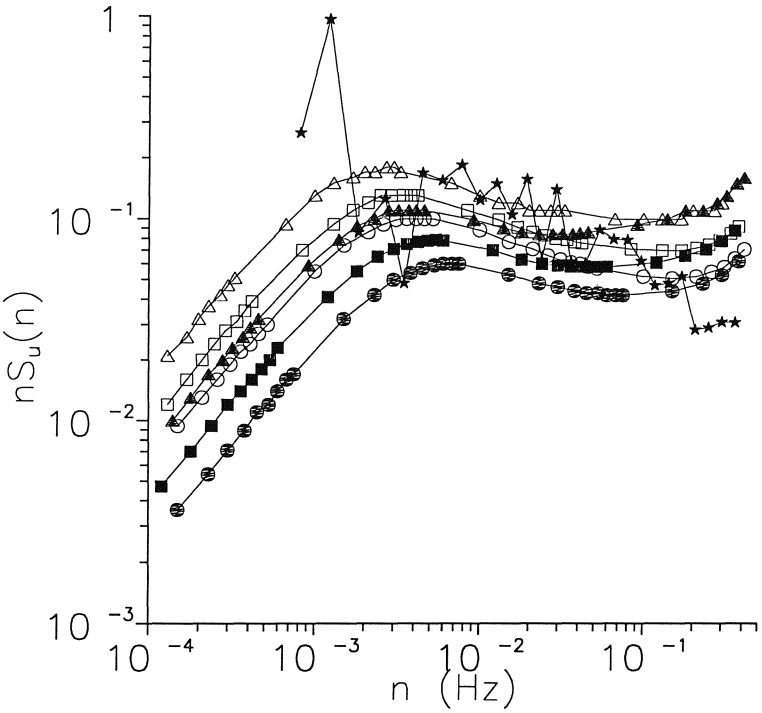

Figure 12. Model and measured spectrum of the u-component of the velocity in the unstable case for sol 554 d1. The sample interval is 1.2 s. For z_i=3,600 m. Corrected model spectra are calculated for the three z_0s and the 2 effective measuring heights. ⋆–⋆ is the measured spectrum. For the model spectra, the symbols are the same as for the u component above.

9 Summary and Conclusions

Spectral analyses of high frequency turbulent boundary layer measurements have been calculated for the Martian atmospheric surface layer for the first time, and compared with state-of-the-art models. The model parameters were derived from similarity theoretical analyses of the mean variations of wind and temperature in the surface layer over the diurnal cycle and by estimates of the surface temperature. The diurnal variation of the heat flux was used to estimate the mixed layer height, required for the models, and to understand the variation with time of day of the inversion height. The generally good agreement between model and measured wind spectra support the validity of similarity theory for Mars.

The measured mean wind at the MSA (Meteorology Sensor Assembly) and the SANMET (Science ANalysis of Meteorology) modeled surface to MSA (0.93 or 1.61 metres) temperature difference were combined to estimate the Richardson number, and from it derive the Obukhov length, L, to obtain stability, z/L, from similarity theory. The similarity estimates of Richardson number are functions of z, z_0, z_{0T}, and L. They are calculated at appropriate measurement heights, z, and for a suite z_0's and were determined by integrating the similarity functions, ϕ_h and ϕ_m to produce estimates of H and u_*. Diurnal variation of these quantities were determined and samples are represented for the time periods for which spectral analyses were completed. It must be remembered that these determinations are dependent on the surface temperature, which is not directly measured, but is modeled by SANMET. Three values of z_0: 0.3, 1.0 and 3.0 cm were used in the calculations and these analyses suggest that z_0 is probably between 1.0 and 3.0 cm, while Sutton *et al.* (1978) suggest 0.1 to 1.0 cm from lander imaging. z_{0T} was then calculated for different values of z_0 and u_* according to formulas from Brutsaert (1982), Appendix D. A fixed value of 0.1 cm was used since the variation with z_0 and u_* was less than 40%. Finally, L was calculated versus time of day from similarity theory. The results resemble the diurnal behavior found by Sutton *et al.* (1978). When the values of the surface layer parameters determined in this process are used in the spectral models for wind and for temperature during stable conditions, the model and measured spectra agree quite well for the limited data analyzed. They demonstrate that the model corrections work and that similarity theory is valid for Mars. Additional analyses can refine the estimates of z_0.

The heat flow into a column was used to derive the height of the convectively mixed layer, $h(t)$, i.e. z_i, versus time of day, assuming the background lapse rate found by Sieff and Kirk (1976) during entry measurements: the lapse rate is clearly a function of location and time, cf. Lindal *et al.* (1979). Maximum daytime depths for specific parameter combinations during early and late spring vary from 3.6 to 9.2 km, Table 4, for the three selected sols, assuming three different values of z_0. The depths calculated here are comparable to those used in the comparison of Haberle's numerical models with similarity derived wind and temperature profiles reported by Tillman (Zurek *et al.*, 1991). Lindal *et al.* (1979) report adiabatic lapse rates up to 6 km at the 22° North VL-1 site, supporting mixed layer depths of much greater than the terrestrial 1–2 km. Orbital imaging observations also suggest depths greater than 2.0 km (Tillman, 1977), and Dust devils have been observed by Thomas and Gierasch (1985), with typical heights of 1–2 km while one reached 6.8 km. Although the mixed layer depths are not independently determined, the use of z_i in the model spectral formulation, and its agreement with the measured spectra, also supports depths of several to 10 km.

The daytime energy balance, and temperature, at the surface is mainly dominated by radiative exchange due to the low Martian density. Consequently, the heat flux for similar radiative conditions from sol to sol is mainly dependent on

the wind speed.

Terrestrial models of the spectrum of wind have been extended to cover a wider range of heights and adjusted for a Kolmorogov length for Mars which is far larger than Earth. Simultaneously, these models have been adjusted to simulate the very severe aliasing produced by the typical measurement scenario, where the sampling rate is as much as an order of magnitude, or more, less than the roll-off frequency of the sensors. With these corrections, the model and measured wind spectra compare quite favorably using reasonable values of z_0 and effective instrument measuring height. The comparisons were better for z_0 values between 1.0 and 3.0 cm, and it is suggested that z_0 is within this range at this site: the roughness length can be further refined by analyzing additional sols. This is an important aspect of this work since it provides an independent check of the bulk parametric procedures used both here and by Sutton *et al.* (1978) and takes advantage for the first time, of analyses of surface layer turbulence. In this process, the dependence of the model spectra on height in the Earth's atmosphere, previously tested only from 3 metres and up, was extended down to 0.93 metre.

Model stable temperature spectra were also created, but only the low frequency part of the spectra showed good agreement. This is most likely due to the need for refinement in the data processing to estimate – and reduce – the effect's noise. For the unstable case, model temperature spectra do not exist.

In general, the comparisons of calculated wind spectra with models were quite good, indicating that Monin-Obukhov similarity holds on Mars as well as Earth, in spite of the absence of an inertial subrange, due to the large Kolmogorov scale for the Martian data. This is supported by the agreement between these estimates of the convective layer depth and others. Conversely, these results imply that these model formulations and extensions should hold on Earth even with a limited or absent inertial subrange, such as might be found very close to a smooth natural boundary, such as dry lake beds, closely cut grass, salt flats, etc. or man made ones such as aircraft skins or a wind tunnel. To be able to demonstrate the absence of the inertial sub range on Earth, would require very small and fast sensors in addition to a smooth surface. The larger Kolmorogov scale of Mars needs to be considered when planning future instruments, measurement suites, and data collection strategies. Finally, Martian surface layer turbulence is associated with much smaller Reynolds numbers than on Earth.

Although the spectral model–measurement comparisons indicate that the surface temperature estimates are reasonable, the main weakness of these conclusions is that the boundary layer parameters depended on the SANMET derived surface temperatures. For example, the estimate of z_0 can be improved by analyzing additional data at the same season, especially under stable conditions and then at different seasons to reduce the scatter of the estimates and verify them with the different seasonal wind directions since the VL-2 site roughness appears to be very uniform from lander images. For VL-1, the roughness is quite dependent on direction as should be evident, if such analyses were carried out.

Acknowledgements

Support from the National Aeronautics and Space Administration for operational, processing and science analyses under several grants is gratefully acknowledged. The assistance of Neal Johnson in software development, and in data processing is appreciated. Conway Leovy's careful review of the manuscript, contributed to its clarification and is greatly appreciated, and we gratefully acknowledge Niels Otto Jensen's clarifying discussions about the surface roughness.

References

Arvidson, R.E., E.A. Guiness, H.J. Moore, J.E. Tillman and S.D. Wall (1982): Three Mars Years: Viking Lander 1 Imaging Observations. *Science*, **222**, 463-468.

Barnes, J.B. (1984): Linear baroclinic instability in the Martian atmosphere. *J. Atmos. Sci.*, **41**, 1536-1550.

Brutsaert, W.H. (1982): *Exchange Processes at the Earth–Atmosphere Interface.* In Engineering meteorology, ed. Erich J. Plate, Elsevier.

Batchelor, G.K. (1967): *An introduction to fluid dynamics.* Cambridge, Chap. 6.

Businger, J.A., J.C. Wyngaard, Y. Izumi, and E.F. Bradley (1971): Flux-profile relationship in the atmospheric surface layer. *J. Atmos. Sci.*, **28**, 181-189.

Chamberlain, T.E., H.L. Cole, R.G. Dutton, G.C. Greene, and J.E. Tillman (1976): Atmospheric measurements on Mars: the Viking Meteorology experiment. *Bull. Amer. Meteo. Soc.*, 1094-1104.

Colburn, D.S., J.B. Pollack, and R.M. Haberle (1989): Diurnal variations in optical depth at Mars. *Icarus*, **79**, 159-189.

Deardorff, J.W. (1979): Prediction of convective mixed-layer entrainment for realistic capping inversion structures. *J. Atmos. Sci.*, **36**, 1070-1076.

Dyer, A.J. (1974): A review of the flux profile relationships. *Boundary Layer Meteorol.*, **7**, 363-372.

Greene, G.C., L.S. Keafer, Jr., C.G. Marple, and J.T. Foughner, Jr. (1972): *Flow-field measurements around a Mars Lander Model Using Hot-Film Anemometers Under Simulated Mars Surface Conditions.* NASA Technical Note TN D-6820, Langley Research Center, Hampton, Va., 23365.

Hess, S.L., R.M. Henry, C.B. Leovy, J.A. Ryan, and J.E. Tillman (1977): Meteorological Results From the Surface of Mars : Viking 1 and 2. *J. of Geophys. Res.*, **82**, 4559-4574.

Højstrup, J. (1982): Velocity spectra in the unstable planetary boundary layer. *J. Atmos. Sci.*, **39**. 2239-2248.

Højstrup, J., S.E. Larsen and P.H. Madsen (1990): Power Spectra of horizontal wind components in the neutral atmospheric surface layer. *Ninth Symposium on turbulence and diffusion.* Amer. Met. Soc., Boston, Mass. 305-308.

Lumley, J.L. and H.A. Panofsky (1964): *The Structure of Atmospheric Turbulence*, John Wiley & Sons.

Kaimal, J.C., J.C. Wyngaard, Y. Izumi and O.R. Coté (1972): Spectral characteristics of surface-layer turbulence. *Quart. J. R. Met. Soc.*, **98**, 563-589.

Kaimal, J.C., J.C. Wyngaard, D.A. Haugen, O.R. Coté, Y. Izumi, S.J. Caughey, and C. J. Ready (1976): Turbulence Structure in the convective boundary layer. *J. Atmos. Sci.*, **33**, 2152.

Kieffer, Hugh H. (1976): Soil and Surface Temperatures at the Viking Landing Sites. *Science*, **194**, 1344-1346.

Larsen, S.E., H.R. Olesen, and J. Højstrup (1985): Parameterization of the low frequency part of spectra of horizontal velocity components in the stable surface boundary layer. *Turbulence and diffusion in stable environments.* J.C.R. Hunt, Ed., Oxford University Press, 181-204.

Leovy, C.B., J.E. Tillman, W.R. Guest and J. Barnes (1985): Interannual Variability of Martian Weather. *Recent Advances in Planetary Meteorology: Proceedings of Seymour Hess Memorial Symposium, IUGG Hamburg 1983,* Garry Hunt, Ed., Cambridge University Press, pp 69-84.

Lindal, G.F., H.B. Holtz, D.N. Sweetnam, Z. Shippony, J.P. Brenkle, G.V. Hartsell and R.T. Spear (1979): Viking Radio Occultation Measurements of the Atmosphere and Topography of Mars: Data Acquired during 1 Martian Year

of Tracking. *J. Geophys. Res*, **84**, B14, 8443-8456.

Murphy, J.R., C.B. Leovy and J.E. Tillman (1990): Observations of Martian Surface Winds at the Viking Lander 1 Site. *J. Geophys. Res.*, **95**, B9, 14,555-14,576.

Nordling, C. and J. Österman (1980): *Physics Handbook.* 2nd edition (1982). Studentlitteratur (Sweden). p. 37.

Olesen, H.R., S.E. Larsen and J. Højstrup (1984): Modeling velocity spectra in the lower part of the planetary boundary layer. *Boundary-Layer Meteorology.*, **29**, 285-312.

Owen, T., K. Biemann, D.R. Rushneck, J.E. Biller, D.W. Howarth, and A.L. Lafleur (1977): The Composition of the Atmosphere at the Surface of Mars. *J. Geophys. Res.*, **82**, 4635-4639.

Ryan, J.A., and R.M. Henry (1979): Mars Atmospheric phenomena during major dust storms, as measured at the surface. *J. Geophys. Res.*, **84**, 2821-2829.

1975: *Viking 75 Project: Software Requirements Document for the Meteorology Analysis Program (SANMET).* for NASA, Langley Research Center, by Martin Marietta Corp., SD-37R0011, Rev. E, 28 Feb.

1975: *Viking 75 Project: Program Description Document for the Meteorology Analysis Program (SANMET).* for NASA, Langley Research Center, by Martin Marietta Corp., SD-37P0011, Rev. A,1 Oct.

1974: *Viking 75 Project: Users Guide for the Meteorology Analysis Program (SANMET).* for NASA, Langley Research Center, by Martin Marietta Corp., SD-37U0011, July.

Sieff, A. and D.B. Kirk (1976): Structure of Mars' atmosphere up to 100 kilometers from the entry measurements of Viking 2. *Science*, **194**, 1300-1302.

Sutton, J.L., C.B. Leovy and J.E. Tillman (1978): Diurnal variation of the martian surface layer meteorological parameters during the first 45 sols at the two Viking lander sites. *J. Atmos. Sci.*, **35**, 2346-2355.

Thomas, P. and P.J. Gierasch (1985): Dust devils on Mars. *Science*, **230**, 175-177.

Tillman, J.E. (1977): Dynamics of the boundary layer of Mars. *Proc. Symposium on Planet. Atmos.*, Roy. Soc. Canada, Ottawa, 145-149.

Tillman, J.E., R.M. Henry, S.L. Hess (1979): Frontal Systems During Passage of the Martian North Polar Hood Over the Viking Lander 2 Site Prior to the First 1977 Dust Storm. *J. Geophys. Res.*, **84**, 2947-2955.

Tillman, J.E. (1988): Mars Global Atmospheric Oscillations: Annually Synchronized, Transient Normal Mode Oscillations and the Triggering of Global Dust Storms, *J. Geophys. Res.*, **93**, D8, 9433-9451.

Tillman, J, L Landberg, and SE Larsen (1994): The Boundary Layer of Mars: Fluxes, Stability, Turbulent Spectra and Growth of the Mixed Layer. *J. of Atmos Sci.*, **51**, 1709-1727.

Davey, R., T.E. Chamberlain and L. Harnett (1973): Viking Meteorology Instrument System *Sensor Design Analysis Report, METC-021*, TRW Systems Group, One Space Park, Redondo Beach Ca., 12 Sept.

Zilitinkevich, S.S. (1975): Resistance Laws and Prediction Equations for the Depth of the Planetary Boundary Layer. *J. Atmos. Sci.*, **32**, 741-752.

Zurek, R.W., J.R. Barnes, R.M. Haberle, J.B. Pollack, J.E. Tillman and C.B. Leovy, in press 1991: *Dynamics of the Atmosphere of Mars* in Mars Book, University of Arizona Press.

A Derivation of expressions for ϕ, U and z_{eff}

The effect on the flow caused by the lander is investigated using theory for potential flow around a sphere, with radius a, in a flow with velocity, U. The velocity in polar coordinates, v_r and v_θ, can be expressed by the measured wind, $|\vec{v}|$, if the polar coordinates (r,θ) of the measuring point are known, cf. Figure 13. They are:

$$\begin{aligned} v_r &= -|\vec{v}|\cos(\theta+\phi) \\ v_\theta &= |\vec{v}|\sin(\theta+\phi) \end{aligned}$$

where ϕ is the angle of deviation of the flow caused by the lander.

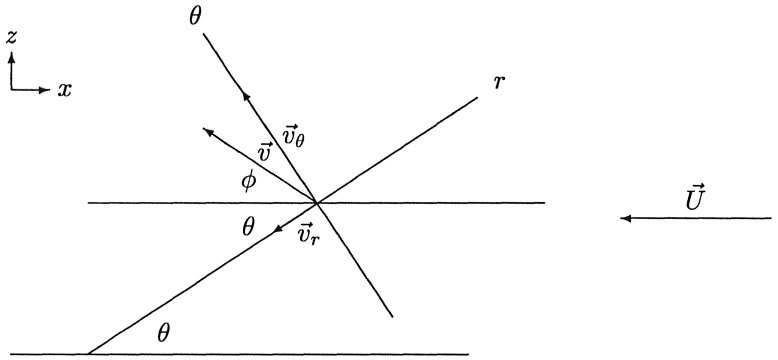

Figure 13. Definition sketch for lander flow distortion.

From photos and drawings of the lander, (Chamberlain *et al.*, 1976), (r,θ) are estimated to be

$$\begin{aligned} a &= 1.6 \text{ m} \\ r &= 2.1 \text{ m} \\ \theta &= 68° \end{aligned}$$

with the stream function given by, (Batchelor, 1967)

$$\psi = -\frac{1}{2}Ur^2\sin^2\theta(1-\frac{a^3}{r^3}) \tag{A.16}$$

the velocities are, respectively

$$\begin{aligned} v_r &= \tfrac{1}{r^2\sin\theta}\tfrac{\partial\psi}{\partial\theta} \\ &= -U\cos\theta(1-a^3/r^3) \end{aligned} \tag{A.17}$$

$$\begin{aligned} v_\theta &= -\tfrac{1}{r\sin\theta}\tfrac{\partial\psi}{\partial r} \\ &= U\sin\theta(1+a^3/2r^3) \end{aligned} \tag{A.18}$$

equating the two expressions for v_r and v_θ, and solving for the two unknowns: U, the free stream velocity, and ϕ, the deviation of the measured wind from horizontal, is

$$U = |\vec{v}|\,\frac{\sin(\theta+\phi)}{\sin\theta(1+a^3/2r^3)} \tag{A.19}$$

and

$$\phi = \tan^{-1}\left[\tan\theta\frac{1+a^3/2r^3}{1-a^3/r^3}\right]-\theta \tag{A.20}$$

Inserting the values of (r,θ) and a in the above expressions gives

$$\begin{aligned} U &= 0.87\,|\vec{v}| \\ \phi &= 11.5^\circ \end{aligned} \tag{A.21}$$

Note that the angle, ϕ, does not depend on the measured velocity, only on the dimensions of the problem.

To estimate the height at which the measured velocity is valid, the streamline is traced back to 'infinity'. The limit of the stream function at infinity is

$$\begin{aligned} \psi_\infty &= -\tfrac{1}{2}Ur^2\sin^2\theta \\ &= -\tfrac{1}{2}Uz^2 \end{aligned}$$

Equating ψ and ψ_∞, the general expression of the undisturbed height of a measurement done at (r,θ) is

$$z = \sqrt{r^2 sin^2\theta(1 - a^3/r^3)}$$

inserting the values of (r,θ) gives

$$z = 1.45 \text{ m}$$

The distance between the center of the sphere and the surface of the earth, $\triangle z$, is 0.52 m, see Figure 2[10]. This means that the height, z_{eff}, where the calculated free stream velocity, U, following the streamline passing through the sensor, is given by

$$\boxed{z_{eff} = z - \triangle z = (1.45 - 0.52) \text{ m} = 0.93 \text{ m}}$$

The wind is considered to advect all other physical quantities. This means that the height, where the measured temperature is valid, is also z_{eff}. In Tables 5 and 6 the values of the parameters, both with lander distortion taken into account, (z_{eff}=0.93), and without, (z_{eff}=1.61), are shown.

Table 5. Parameter values on sol 30 and 447 for z_0=1.0 cm.

		Sol 30	Sol 447		
		n3	d1	n1	n2
L,	z=0.93	93	-18	7	14
	z=1.61	107	-16	10	11
u_*,	z=0.93	0.20	0.35	0.08	0.10
	z=1.61	0.21	0.37	0.08	0.10
H,	z=0.93	-0.22	11.3	-0.23	-0.28
	z=1.61	-0.21	11.0	-0.18	-0.22
U,	measured	3.4	4.4	1.2	1.4
U,	free-stream	3.0	3.8	1.1	1.2
	T_{surf}	194	236	186	184
	T_{atm}	195	214	188	187

The derivations above, where the flow comes directly through the sensors, is easily extended to arbitrary flow directions. In general, the angle theta is the angle between the incoming horizontal wind vector attacking in the center of the sphere and the vector from this center to the position of the sensor. Hence:

$$\cos\theta = \frac{\cos\theta_0}{\sqrt{1 + \left(\frac{h}{r}\right)^2}} \tag{A.22}$$

[10]Measured from the photo and drawings (Chamberlain *et al.*, 1976)

Table 6. Parameter values used on sol 448 and 554 for z_0=1.0 cm.

		Sol 448						Sol 554	
		d1	d2	d3	n1	n2	n3	d1	d2
L,	z=0.93	-53	-53	-84	32	18	17	-9.3	-7.6
	z=1.61	-46	-48	-83	26	15	14	-8.2	-6.7
u_*,	z=0.93	0.61	0.65	0.72	0.20	0.13	0.11	0.26	0.24
	z=1.61	0.63	0.67	0.74	0.20	0.12	0.11	0.28	0.25
H,	z=0.93	19.9	24.2	20.2	-1.00	-0.47	-0.34	10.6	9.5
	z=1.61	18.8	22.8	18.8	-0.87	-0.39	-0.28	10.5	9.5
U,	measured	7.8	8.4	9.3	2.6	1.8	1.6	3.2	2.9
U,	free-stream	6.8	7.3	8.1	2.3	1.6	1.4	2.8	2.5
	T_{surf}	236	243	245	193	191	189	259	261
	T_{atm}	213	217	225	197	193	191	233	236

where θ_0 is the angle of the wind and h is the nominal height of the sensor. Substitution of (A.22) into the equations above, yields the azimuth dependency of the lander distortion of the wind vector as shown on Figs. 14 and 15. The ratio between the the lander distorted wind and the upstream is seen to vary between 1.0 and 1.2 for the azimuth angles of interest here. These bounds on the flow distortion are, however, compounded by other uncertainties, i.e. the simplicity of our description and the fact that the wind tunnel studies of the lander influence actually yielded values between 0.96 and 1.0, see discussion in Section 4. Based on these considerations, we have chosen to perform the data analysis corresponding to two different flow distortion situations. a) No flow distortion meaning that the lander measures the true wind velocity at the true height and b) the measured velocity is 1.15 times the free stream velocity and the corresponding free stream line height is equal to 0.93 m.

B SANMET surface temperature calculations

SANMET is short for Science ANalysis of METeorology and is the software developed by the prime contractor, Martin Marietta Corp., the sub contractor for the meteorology instrument, TRW, and the Viking Meteorology Team. SANMET (SANMET1 (1975), SANMET2 (1975) and SANMET3 (1974)), checks the data from the Viking Landers for errors against limits, converts raw instrument bits to engineering data, and then combines the outputs of several engineering parameters to obtain Science results. Among the many enhancements and additions at UW, it produces estimates of the surface temperature, using techniques developed by Ronnholm and Leovy, private communication, to provide radiative corrections for the temperatures calculated by the wind reference temperature sensor. Radiative flux estimates are used to correct for radiative errors in the wind reference temperature sensor, and to a lesser extent the ambient thermocouple sensor. Due to its small 75 μ diameter, the separation of the thermocouple junction from the support structure, and the carefully chosen exposure and mounting, the conduction and radiation errors of the thermocouple ambient temperature sensor are small. The correction process involves calculating a diurnally varying surface temperature, which is subsequently used, with the surface emissivity, to estimate the upward long wave flux. The downward and upward solar and infrared fluxes at the sur-

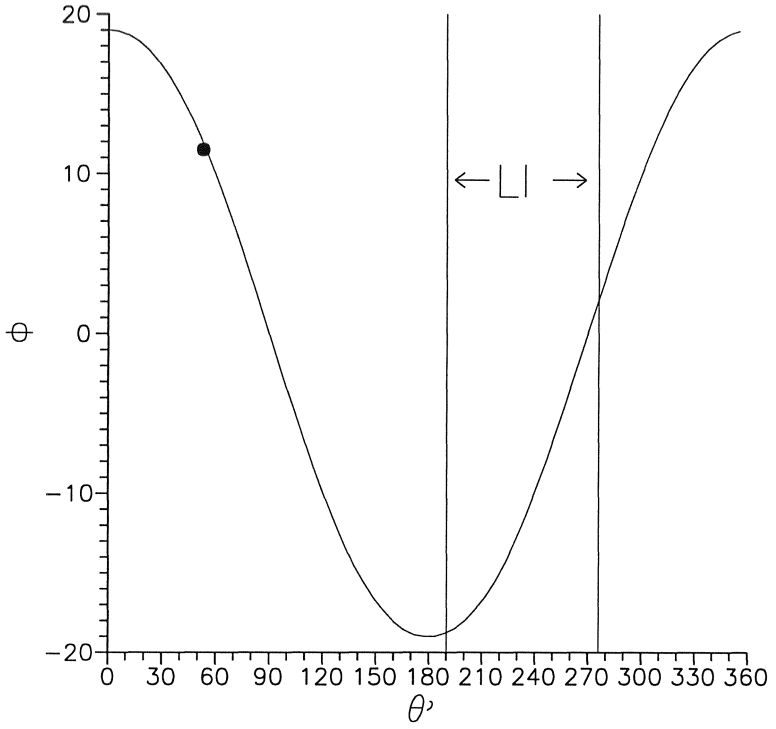

Figure 14. The relative deviation of the wind direction, ϕ (as compared to the free-stream wind speed) caused by the lander as a function of the angle of incidence, θ' of the incoming flow. The region between the two vertical lines marked 'LI' is the region of lander interference, i.e. the region where the flow comes from the lander before it reaches the instrument. The situation where the flow comes radially from the instrument to the lander is marked with a •.

face, along with the surface temperature, are calculated. Optical depth values are obtained from Colburn *et al.* (1989) on a sol–by–sol basis, and surface albedo, thermal inertia, air density, asymmetry parameter, single scattering albedo and thermal emissivity of dust, are also components of the calculation. Solar geometry and fluxes are calculated using a δ-Eddington 1 layer atmosphere. Downward infrared fluxes are calculated using seasonally varying diurnally uniform sky temperatures, estimated and interpolated from a variety of data sources and model calculations. Finally, ground temperatures are calculated for a single layer thermal conductivity model for a periodic (diurnal) heat source using a Fourier solution.

C Calculation of ρ and c_p at the surface of Mars

In order to derive ρ and c_p, the gas constant, R, of the Martian atmosphere is required. It is defined by

$$R = R^*/M$$

where R^* is the universal gas constant (=8314.3 J K^{-1} $kmol^{-1}$) and M is the molecular weight of the gas in kg $kmol^{-1}$. Assuming that the atmosphere contains of CO_2 (molecular weight 12.01 + 2·16.00 = 44.01 kg $kmol^{-1}$) exclusively, the gas constant is 188.92 J K^{-1} kg^{-1}.

Given the gas constant, the specific heat at constant pressure, c_p, is given by

$$c_p = c_v + R$$

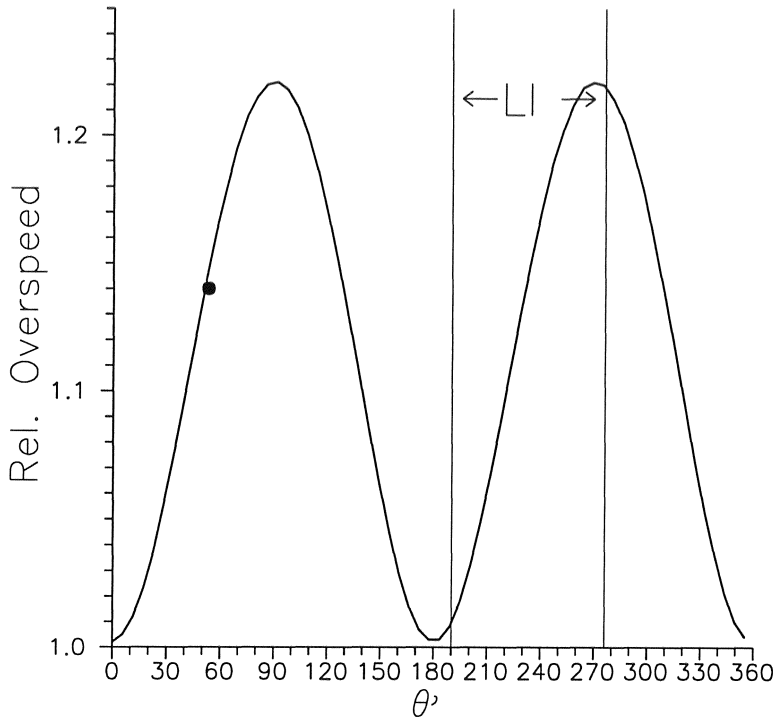

Figure 15. The relative overspeed of the wind speed (as compared to the free-stream wind speed) caused by the lander as a function of the angle of incidence, θ' of the incoming flow. The region between the two vertical lines marked 'LI' is the region of lander interference, i.e. the region where the flow comes from the lander before it reaches the instrument. The situation where the flow comes radially from the instrument to the lander is marked with a •.

where c_v is the specific heat at constant volume. The ratio of c_p to c_v is 1.30, cf. Nordling and Österman (1980), leading to that

$$\boxed{c_p = 818.65 \text{ J K}^{-1}\text{kg}^{-1}}$$

The density, ρ, can be deduced from the ideal gas law

$$\rho = p/RT$$

Using the pressure at the surface of Mars of Sieff and Kirk (1976) of 7.75 mb, a typical atmospheric temperature of 220 K, gives

$$\boxed{\rho = 0.019 \text{ kg m}^{-3}}$$

D Determination of z_{0T}

The roughness length, z_0, pertaining to the logarithmic wind profile is a measure for the flux of momentum to the surface at a given wind speed. Similarly the temperature "roughness" length, z_{0T}, is associated with a logarithmic profile and the heat flux pertaining to a given vertical temperature gradient. Corresponding to z_0, z_{0T} is the height where the extrapolated logarithmic profile attains the surface temperature value, T_0. Hence, the magnitude of the different z_0's are controlled by the transport mechanisms very close to the surface, where molecular processes are important. The processes driving the heat flux lack the mechanism of form drag around roughness elements that is available for the transfer of momentum, and the value of z_{0T} is generally less than z_0.

Considering a two layer heat flux model, an upper turbulent surface layer (I), and a lower layer adjacent to the surface controlled by molecular transport (II) the heat flux, H, can be expressed as:

$$-H = ku_*(T_\Delta - T_0)/\ln(\frac{\Delta}{z_{0T}}) \tag{D.23}$$

$$-H = \kappa(T_\Delta - T_0)/\Delta \tag{D.24}$$

where Δ is the intersection height for the two layers
Using D.23 and D.24 and $\ln \Delta/z_{0T} = \ln \frac{\Delta}{z_0} + \ln z_0/z_{0T}$, gives

$$\ln z_0/z_{0T} \equiv kX \quad (D1)$$

where

$$kX \equiv \frac{ku_*}{\kappa}\Delta - \ln \frac{\Delta}{z_0}$$

$z_{0T} = z_0 \exp(-kX)$

The behavior of X has frequently been described, generally formulated in terms of $X = X(Pr = \nu/\kappa, Re = u_* z_0/\nu)$. For example, Brutsaert (1982), calculates the behavior of X as follows

$$X(\mathrm{Re}_0, \mathrm{Pr/Sc}) = 7.3\mathrm{Re}_0^{1/4}\mathrm{Sc}^{1/2}$$

where $\mathrm{Re}_0 = u_* z_0/\nu$.

In the present data set u_* ranges between 0.1 and 0.9 m/s. In the present analysis three alternative z_0 values, 3, 1 and 0.3 cm. are used. Assuming $Pr \simeq 1$ all three z_0 values are found to yield z_{0T} around 0.1 cm with some variation with u_*. In the analysis in this paper this variability is neglected and it is assumed that $z_{0T} = 0.1$ cm for all z_0-values, tested.

E Growth of the boundary layer

In this Appendix the daily variation of the height of the boundary-layer will be given for each of the sols with unstable runs. The model is described in Section 6.

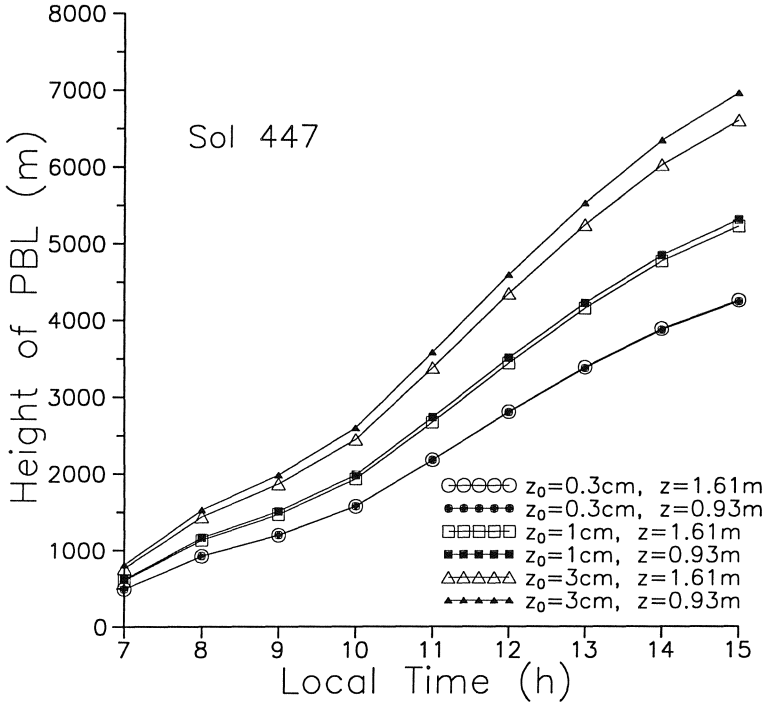

Figure 16. The height of the lowest inversion given as a function of local time of day for sol 447.

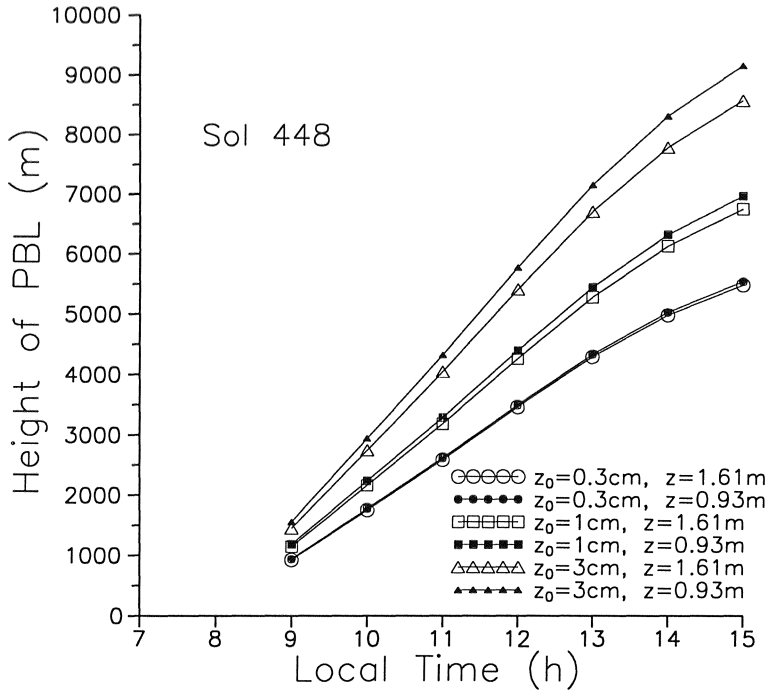

Figure 17. The height of the lowest inversion given as a function of local time of day for sol 448.

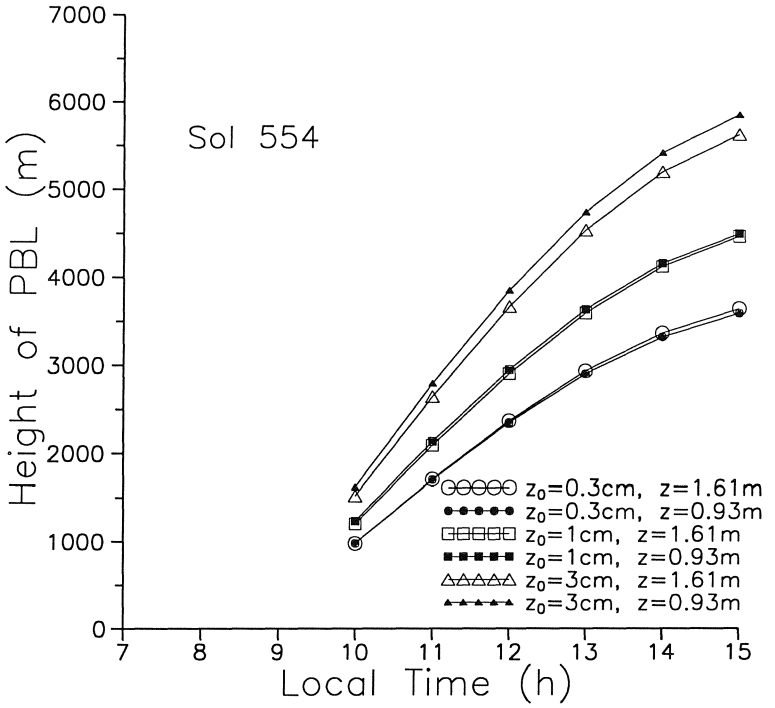

Figure 18. The height of the lowest inversion given as a function of local time of day for sol 554.

F Plots of the spectra

Spectra that have not been discussed in the text are presented to allow the evaluation of the accuracy of the conclusion that model and measured spectra are in good agreement and that the range of surface layer parameters proposed are reasonable. Plots of the time series for these sols are presented including expanded versions of the segments tabulated. Presentation of these comparisons is important as they are the first spectra of Martian boundary layer turbulence published and the determination of the best fit to the surface roughness and effective measuring height currently are subjective. Objective methods have been proposed but are beyond the scope of this program.

F.1 Stable cases

u-spectra

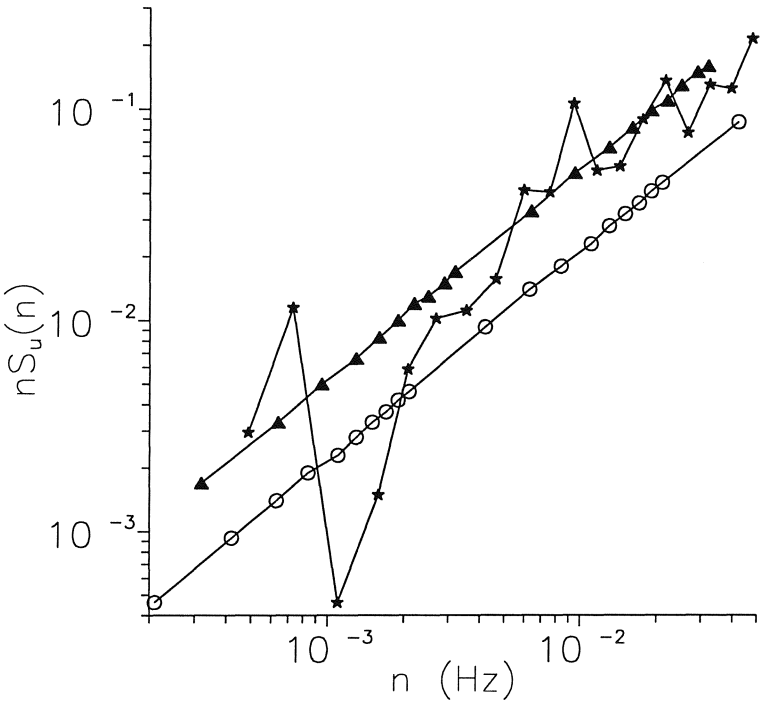

Figure 19. The stable u-spectrum from sol 30, n3, compared to the model with z=1.61 m and z_0= 0.3 cm (marked with open circles) and the model with z=0.93 m and z_0= 3.0 cm (marked with filled triangles).

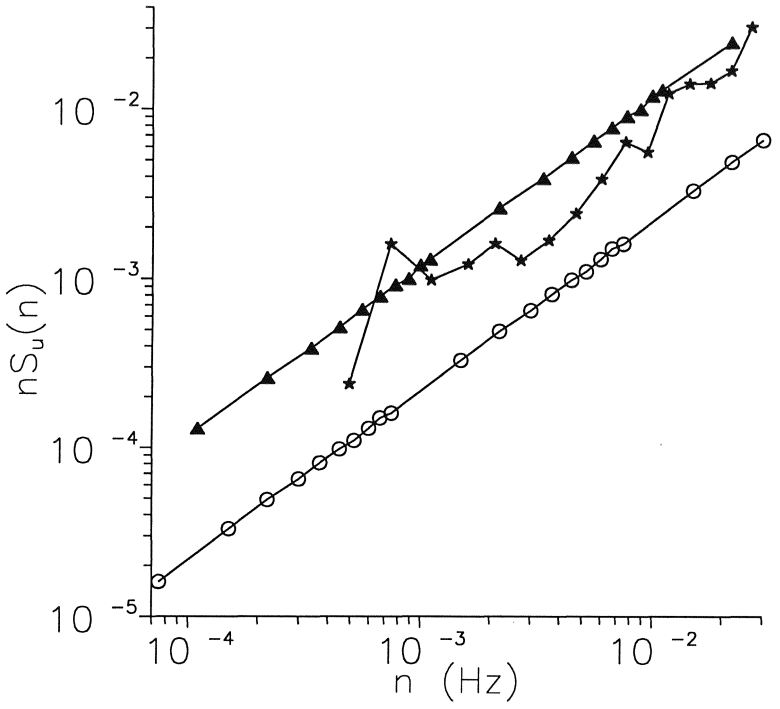

Figure 20. The stable u-spectrum from sol 447, n1, compared to the model with z=1.61 m and z_0= 0.3 cm (marked with open circles) and the model with z=0.93 m and z_0= 3.0 cm (marked with filled triangles).

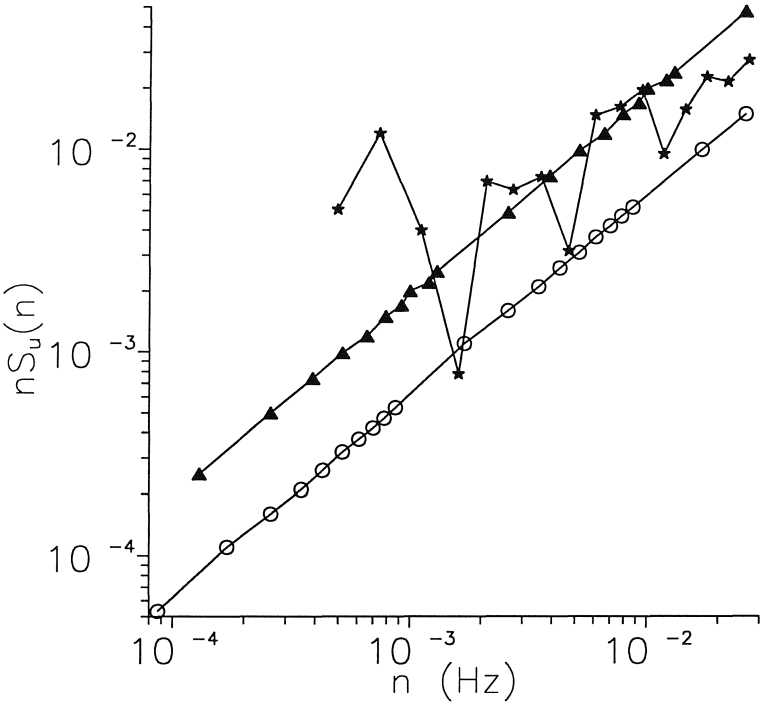

Figure 21. The stable u-spectrum from sol 447, n2, compared to the model with z=1.61 m and z_0= 0.3 cm (marked with open circles) and the model with z=0.93 m and z_0= 3.0 cm (marked with filled triangles).

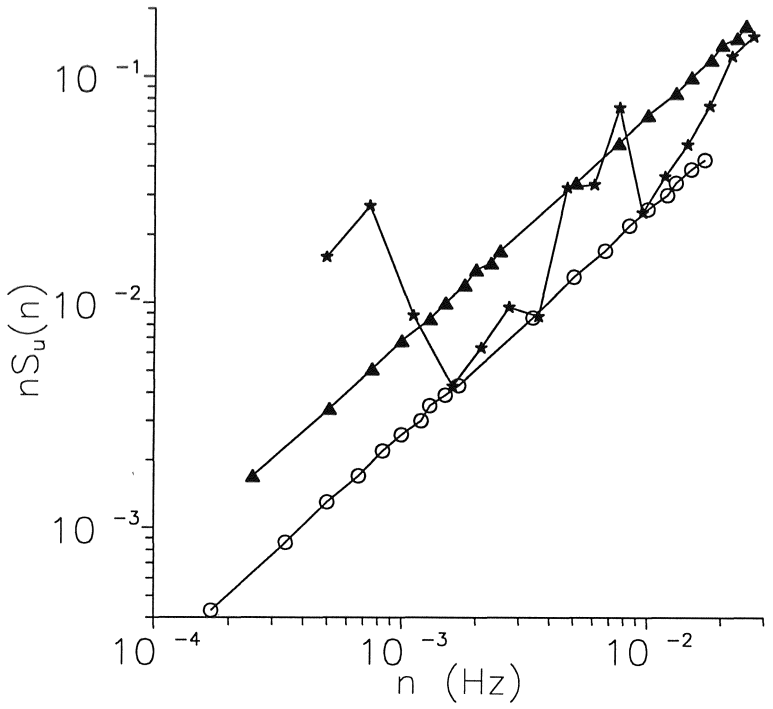

Figure 22. The stable u-spectrum from sol 448, n1, compared to the model with z=1.61 m and z_0= 0.3 cm (marked with open circles) and the model with z=0.93 m and z_0= 3.0 cm (marked with filled triangles).

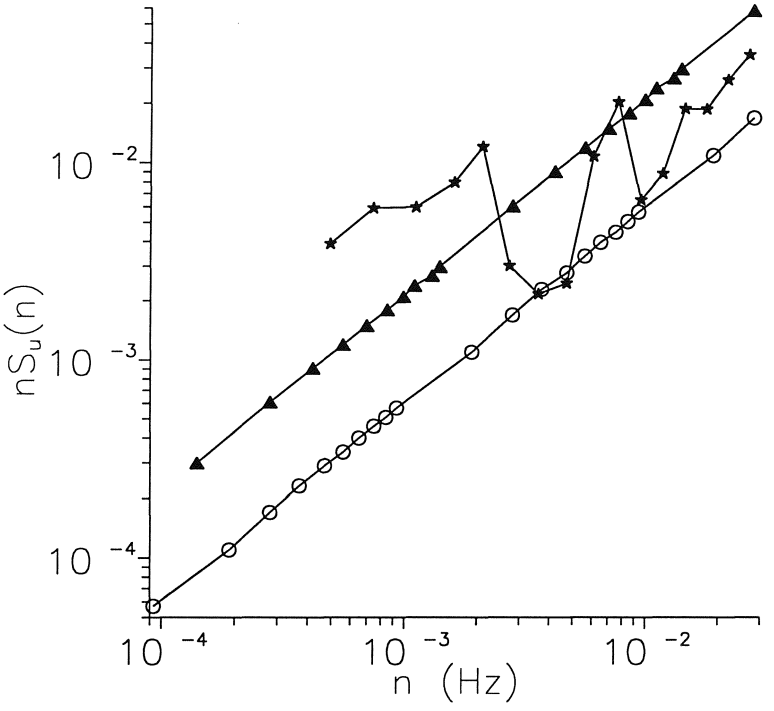

Figure 23. The stable u-spectrum from sol 448, n3, compared to the model with z=1.61 m and z_0= 0.3 cm (marked with open circles) and the model with z=0.93 m and z_0= 3.0 cm (marked with filled triangles).

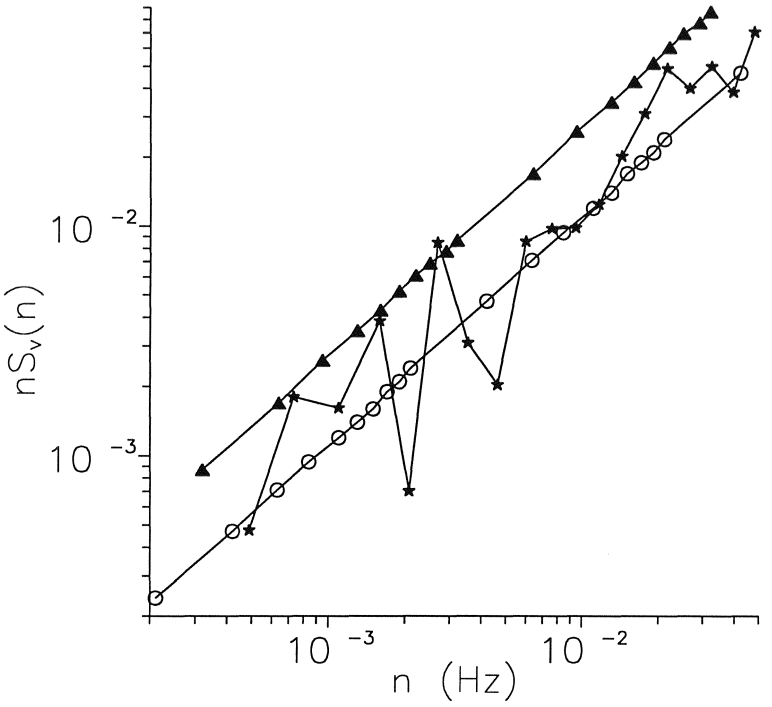

Figure 24. The stable v-spectrum from sol 30, n3, compared to the model with z=1.61 m and z_0= 0.3 cm (marked with open circles) and the model with z=0.93 m and z_0= 3.0 cm (marked with filled triangles).

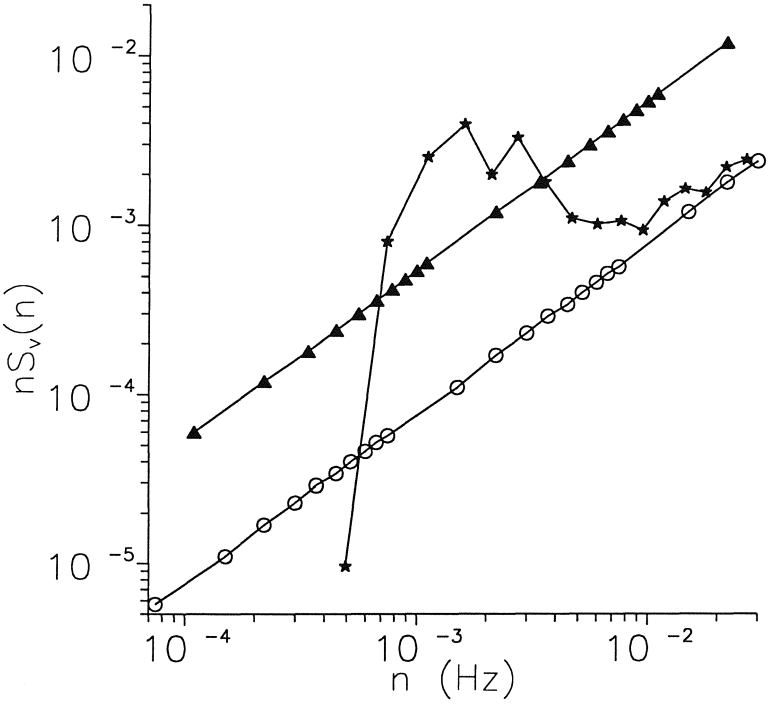

Figure 25. The stable v-spectrum from sol 447, n1, compared to the model with z=1.61 m and z_0= 0.3 cm (marked with open circles) and the model with z=0.93 m and z_0= 3.0 cm (marked with filled triangles).

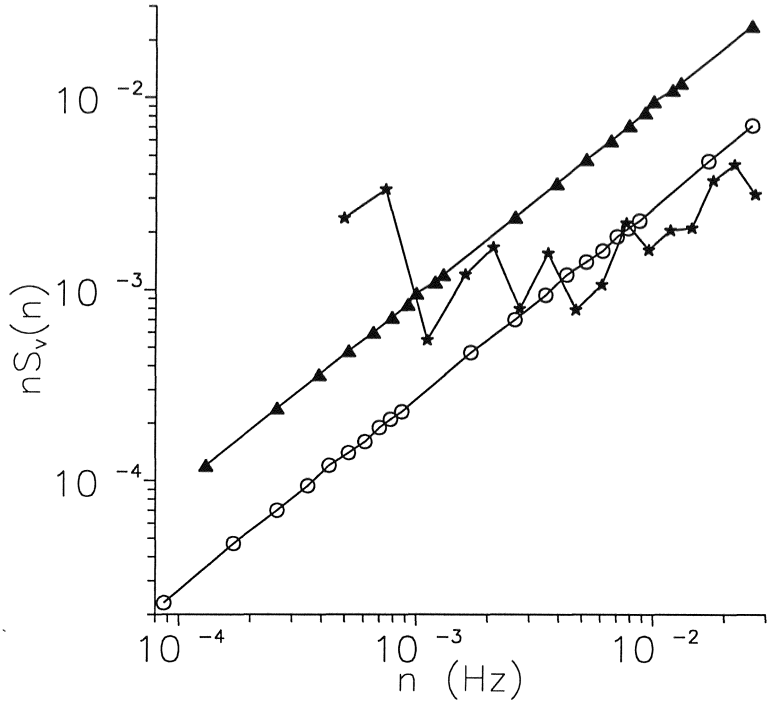

Figure 26. The stable v-spectrum from sol 447, n2, compared to the model with z=1.61 m and z_0= 0.3 cm (marked with open circles) and the model with z=0.93 m and z_0= 3.0 cm (marked with filled triangles).

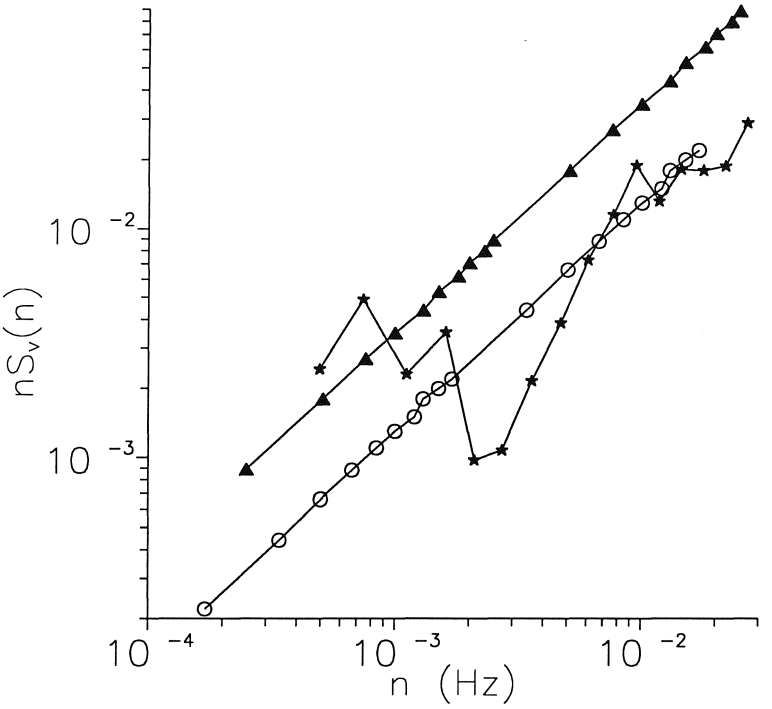

Figure 27. The stable v-spectrum from sol 448, n1, compared to the model with z=1.61 m and z_0= 0.3 cm (marked with open circles) and the model with z=0.93 m and z_0= 3.0 cm (marked with filled triangles).

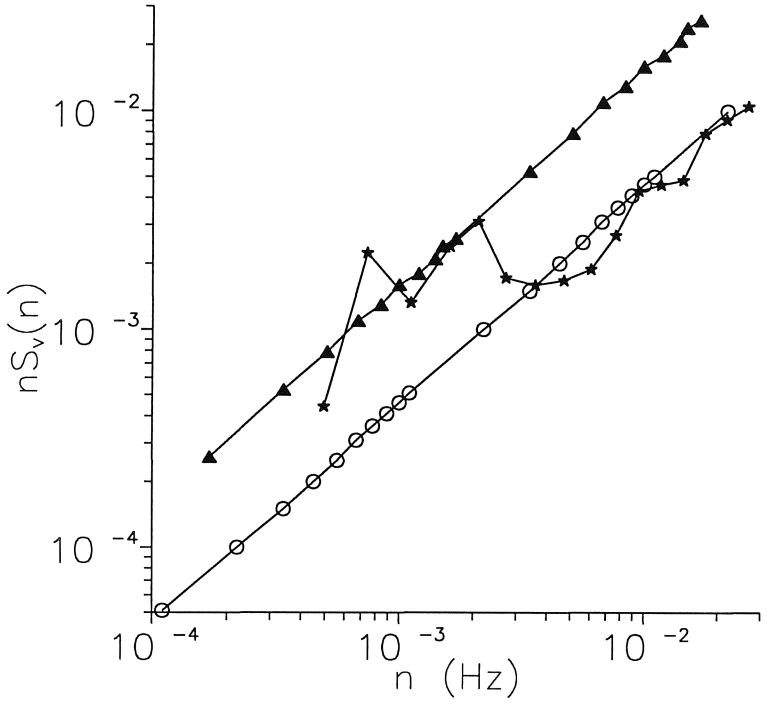

Figure 28. The stable v-spectrum from sol 448, n2, compared to the model with z=1.61 m and z_0= 0.3 cm (marked with open circles) and the model with z=0.93 m and z_0= 3.0 cm (marked with filled triangles).

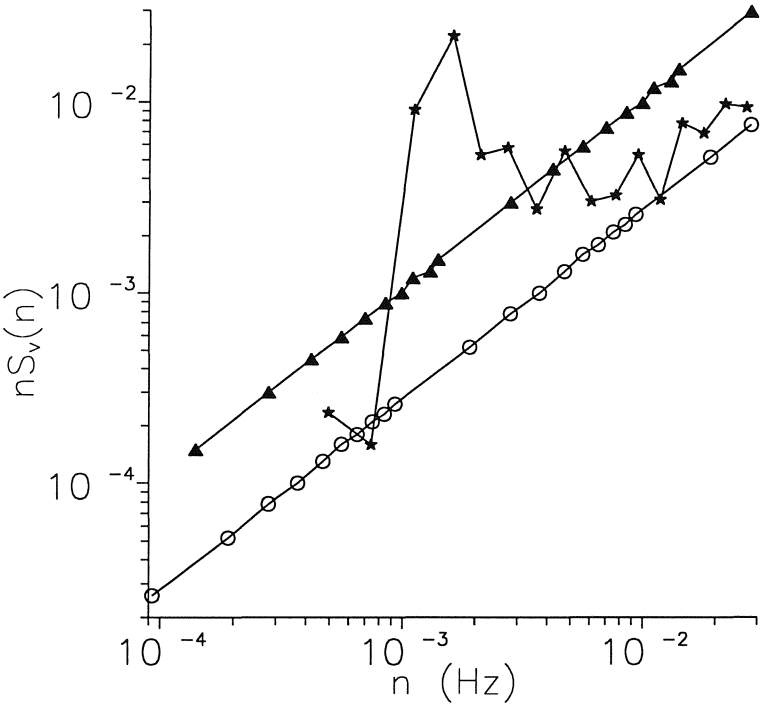

Figure 29. The stable v-spectrum from sol 448, n3, compared to the model with z=1.61 m and z_0= 0.3 cm (marked with open circles) and the model with z=0.93 m and z_0= 3.0 cm (marked with filled triangles).

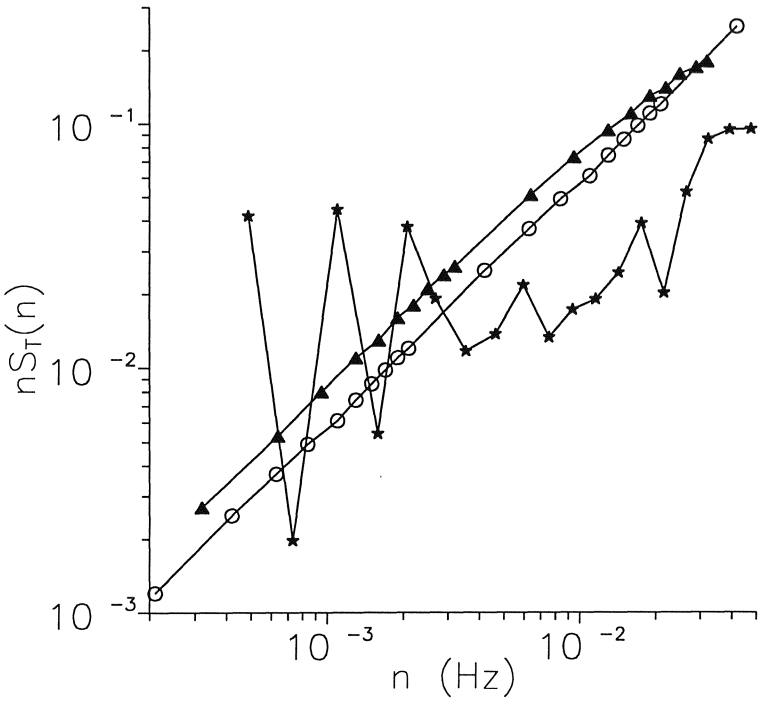

Figure 30. The stable T-spectrum from sol 30, n3, compared to the model with z=1.61 m and z_0= 0.3 cm (marked with open circles) and the model with z=0.93 m and z_0= 3.0 cm (marked with filled triangles).

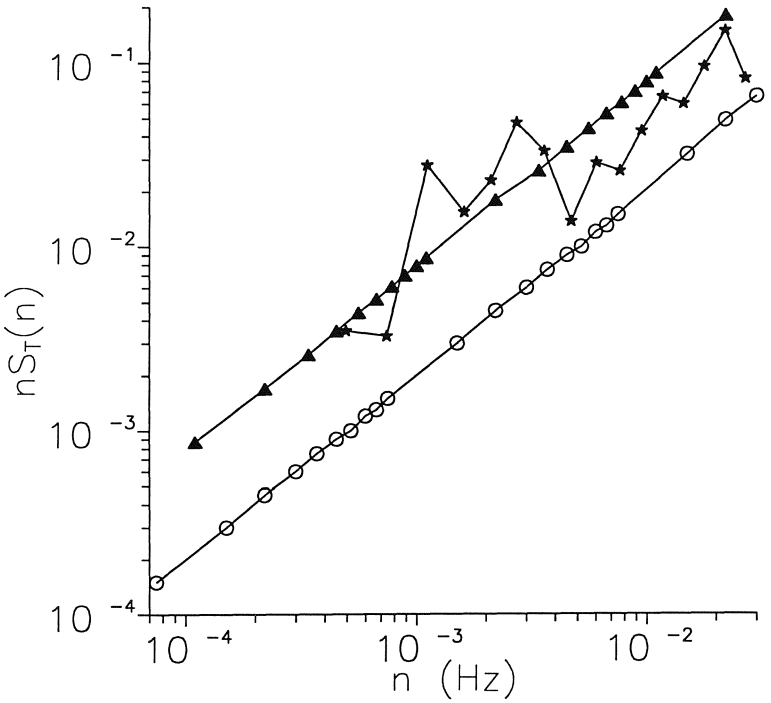

Figure 31. The stable T-spectrum from sol 447, n1, compared to the model with z=1.61 m and z_0= 0.3 cm (marked with open circles) and the model with z=0.93 m and z_0= 3.0 cm (marked with filled triangles).

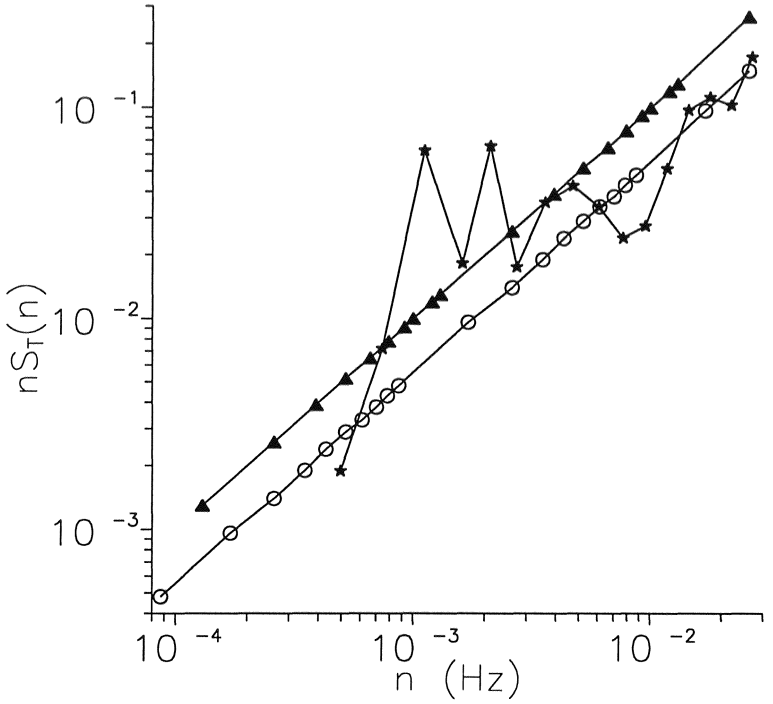

Figure 32. The stable T-spectrum from sol 447, n2, compared to the model with z=1.61 m and z_0= 0.3 cm (marked with open circles) and the model with z=0.93 m and z_0= 3.0 cm (marked with filled triangles).

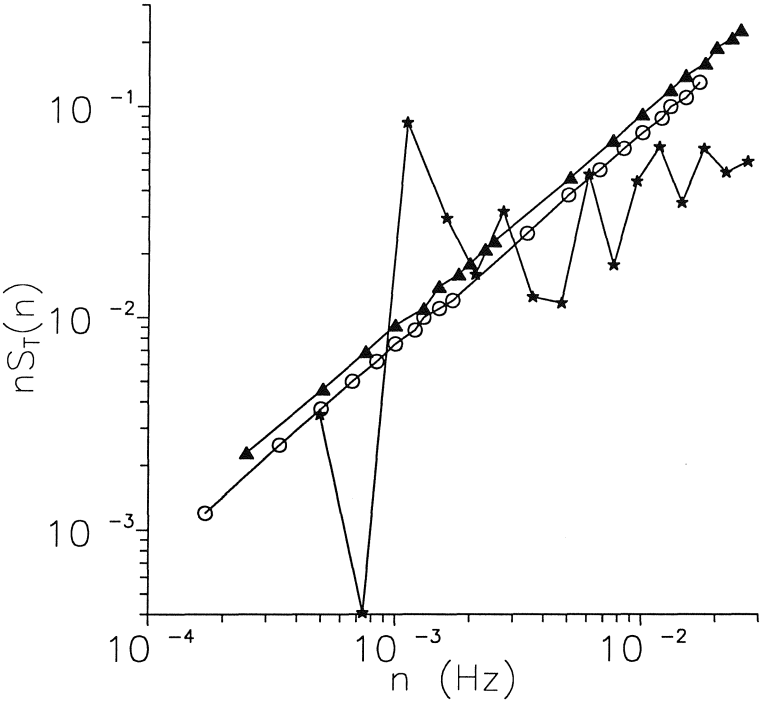

Figure 33. The stable T-spectrum from sol 448, n1, compared to the model with z=1.61 m and z_0= 0.3 cm (marked with open circles) and the model with z=0.93 m and z_0= 3.0 cm (marked with filled triangles).

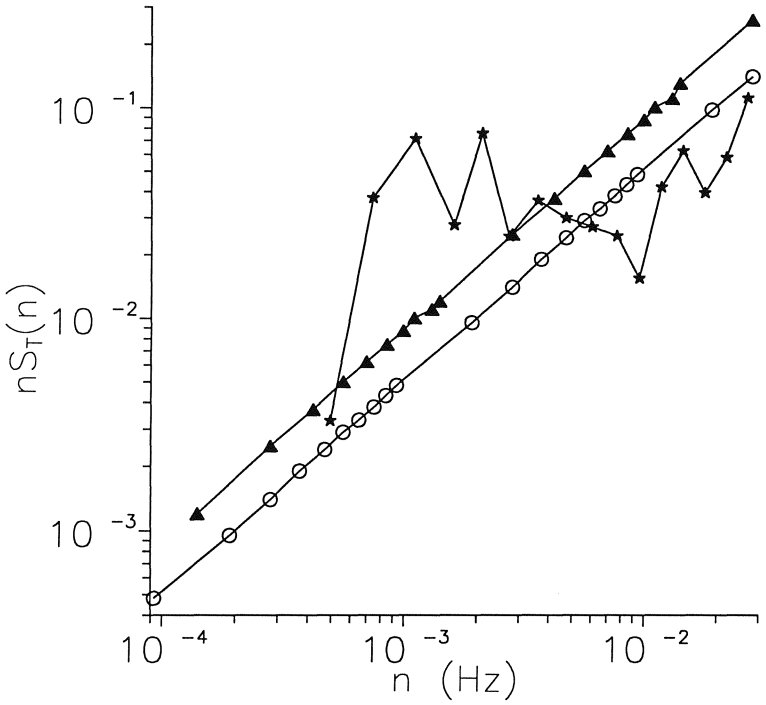

Figure 34. The stable T-spectrum from sol 448, n3, compared to the model with z=1.61 m and z_0= 0.3 cm (marked with open circles) and the model with z=0.93 m and z_0= 3.0 cm (marked with filled triangles).

F.2 Unstable cases

u-spectra

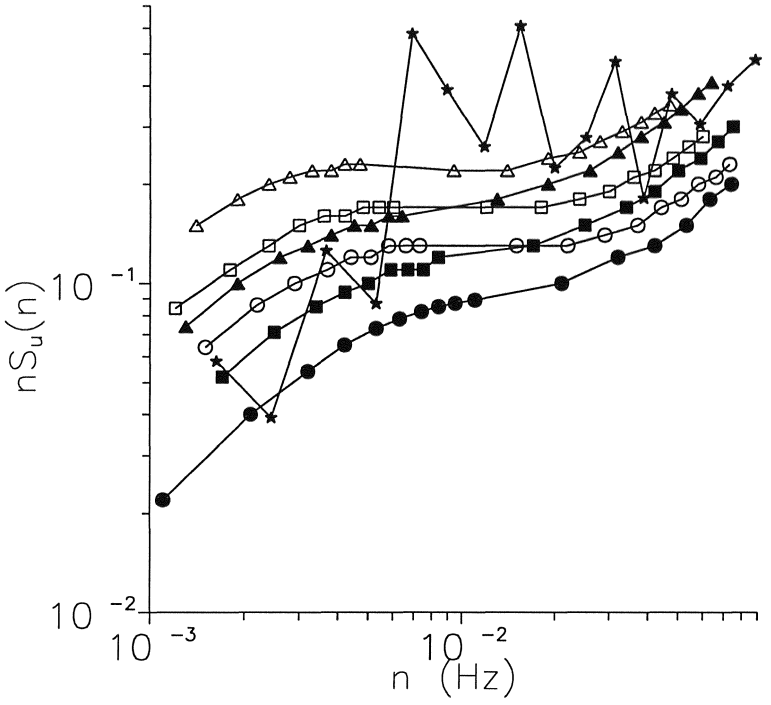

Figure 35. Model and measured spectrum of the u-component of the velocity in the unstable case, for sol 447, d1. Corrected, model spectra are calculated for the three z_0's and two effective measuring heights. ⋆–⋆ is the measured spectrum. For the model spectra, the symbols for the z_0's are: ○ 0.3 cm, □ 1.0 cm, △ 3.0 cm. Solid symbols indicate a height, z, of 0.93 m while open symbols indicate a height of 1.61 m.

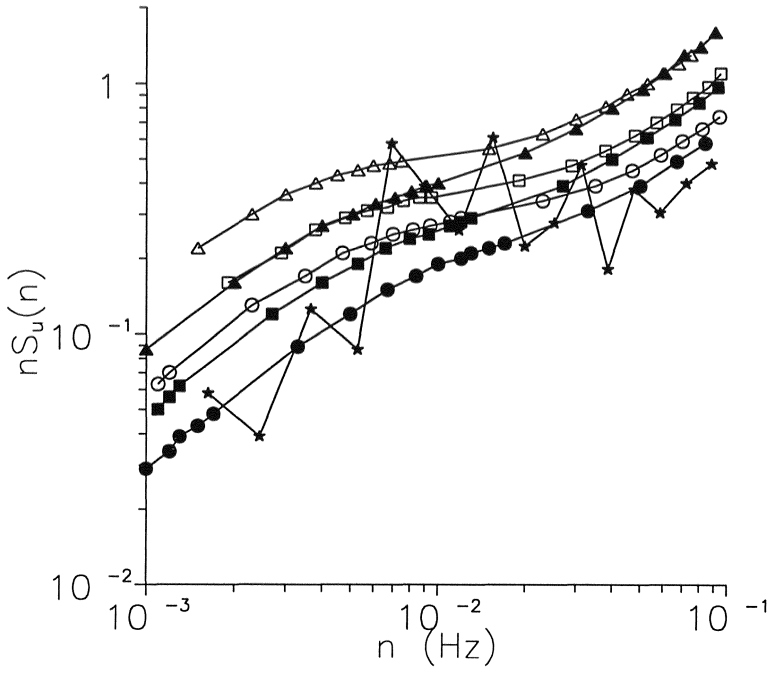

Figure 36. Model and measured spectrum of the u-component of the velocity in the unstable case, for sol 448, d1. Corrected, model spectra are calculated for the three z_0's and two effective measuring heights. ⋆–⋆ is the measured spectrum. For the model spectra, the symbols for the z_0's are: ○ 0.3 cm, □ 1.0 cm, △ 3.0 cm. Solid symbols indicate a height, z, of 0.93 m while open symbols indicate a height of 1.61 m.

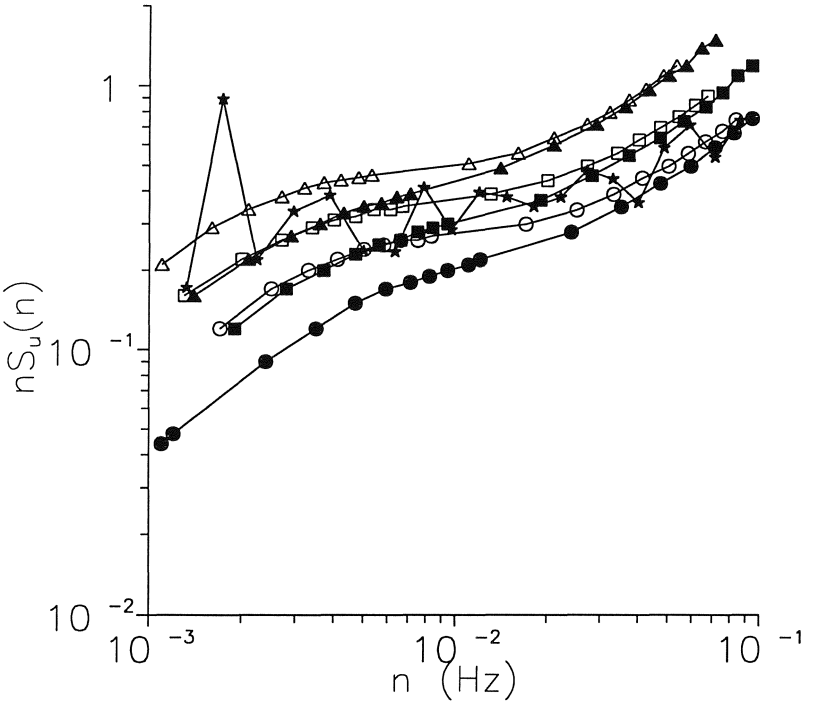

Figure 37. Model and measured spectrum of the u-component of the velocity in the unstable case, for sol 448, d3. Corrected, model spectra are calculated for the three z_0's and two effective measuring heights. ⋆–⋆ is the measured spectrum. For the model spectra, the symbols for the z_0's are: ○ 0.3 cm, □ 1.0 cm, △ 3.0 cm. Solid symbols indicate a height, z, of 0.93 m while open symbols indicate a height of 1.61 m.

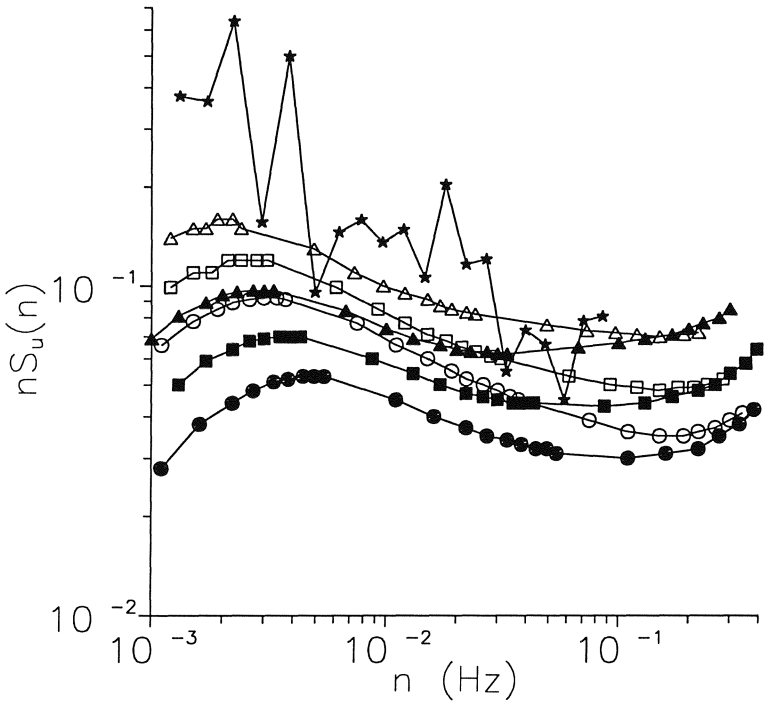

Figure 38. Model and measured spectrum of the u-component of the velocity in the unstable case, for sol 554, d2. Corrected, model spectra are calculated for the three z_0's and two effective measuring heights. ⋆–⋆ is the measured spectrum. For the model spectra, the symbols for the z_0's are: ○ 0.3 cm, □ 1.0 cm, △ 3.0 cm. Solid symbols indicate a height, z, of 0.93 m while open symbols indicate a height of 1.61 m.

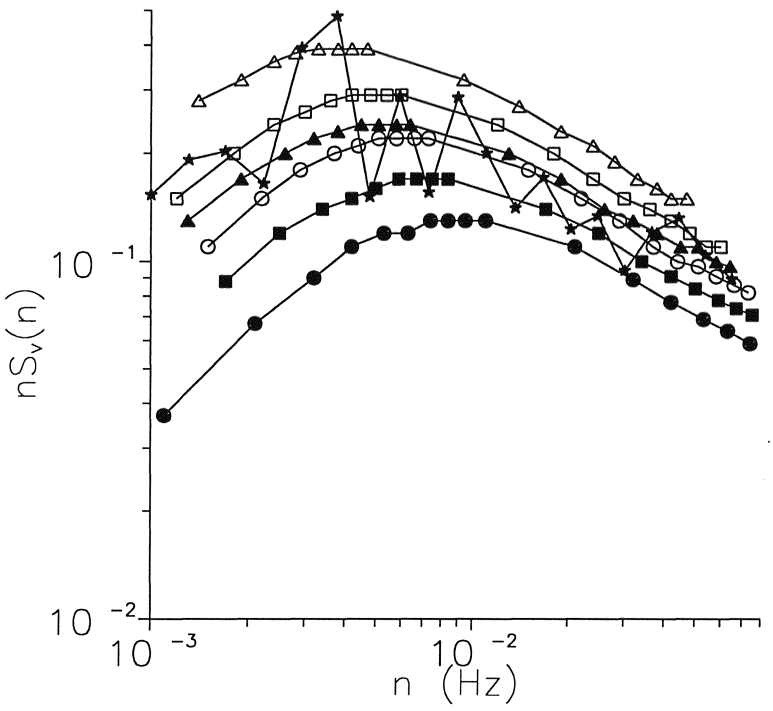

Figure 39. Model and measured spectrum of the v-component of the velocity in the unstable case, for sol 447, d1. Corrected, model spectra are calculated for the three z_0's and two effective measuring heights. ⋆–⋆ is the measured spectrum. For the model spectra, the symbols for the z_0's are: ○ 0.3 cm, □ 1.0 cm, △ 3.0 cm. Solid symbols indicate a height, z, of 0.93 m while open symbols indicate a height of 1.61 m.

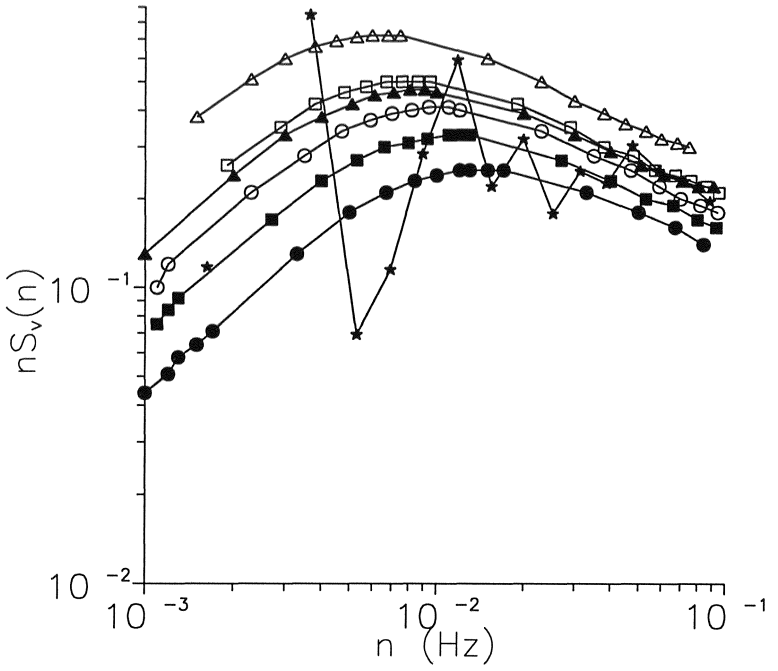

Figure 40. Model and measured spectrum of the v-component of the velocity in the unstable case, for sol 448, d1. Corrected, model spectra are calculated for the three z_0's and two effective measuring heights. ⋆–⋆ is the measured spectrum. For the model spectra, the symbols for the z_0's are: ○ 0.3 cm, □ 1.0 cm, △ 3.0 cm. Solid symbols indicate a height, z, of 0.93 m while open symbols indicate a height of 1.61 m.

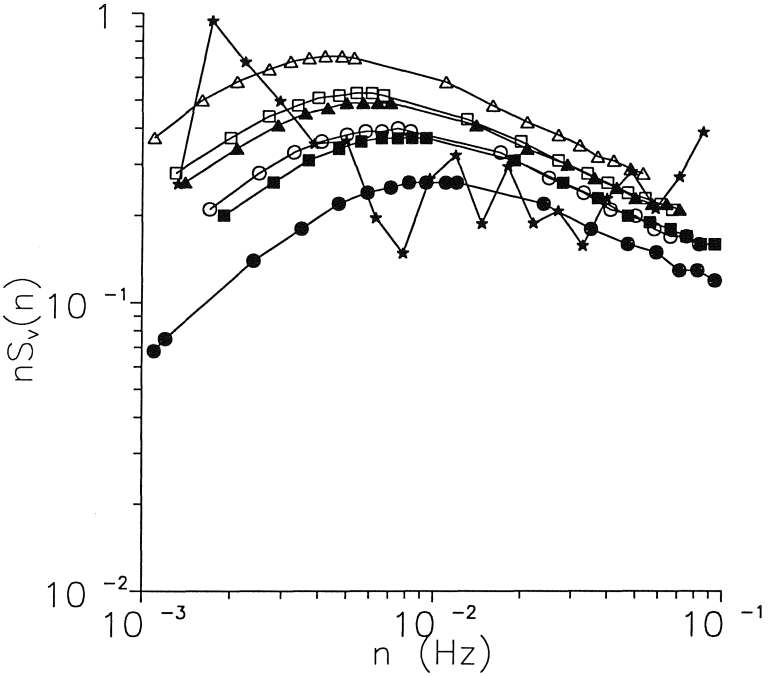

Figure 41. Model and measured spectrum of the v-component of the velocity in the unstable case, for sol 448, d3. Corrected, model spectra are calculated for the three z_0's and two effective measuring heights. ⋆–⋆ is the measured spectrum. For the model spectra, the symbols for the z_0's are: ○ 0.3 cm, □ 1.0 cm, △ 3.0 cm. Solid symbols indicate a height, z, of 0.93 m while open symbols indicate a height of 1.61 m.

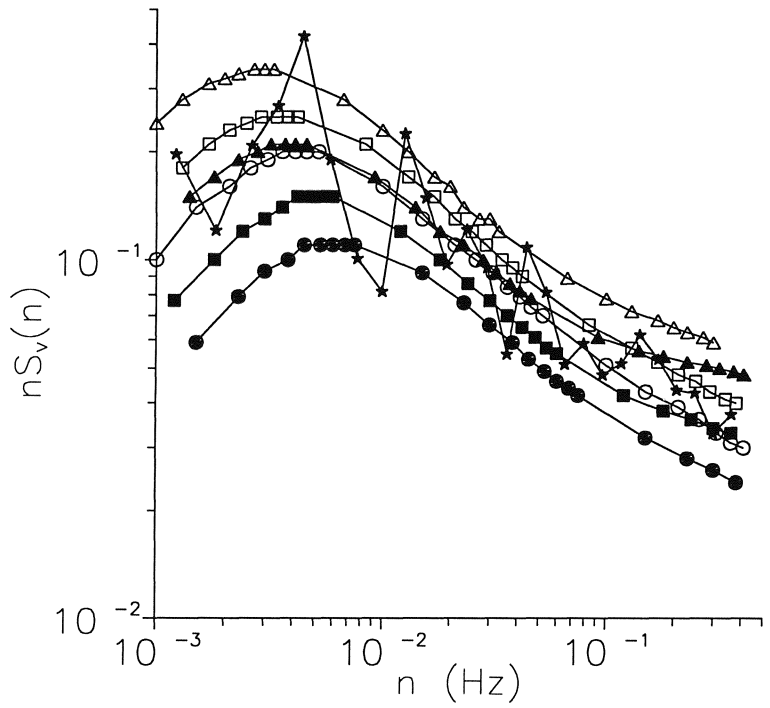

Figure 42. Model and measured spectrum of the v-component of the velocity in the unstable case, for sol 554, d1. Corrected, model spectra are calculated for the three z_0's and two effective measuring heights. ⋆–⋆ is the measured spectrum. For the model spectra, the symbols for the z_0's are: ○ 0.3 cm, □ 1.0 cm, △ 3.0 cm. Solid symbols indicate a height, z, of 0.93 m while open symbols indicate a height of 1.61 m.

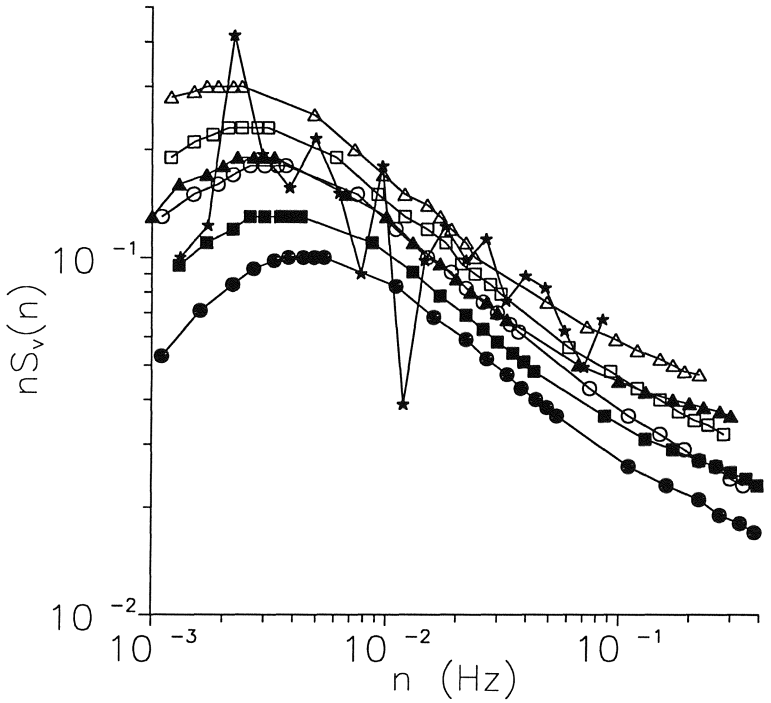

Figure 43. Model and measured spectrum of the v-component of the velocity in the unstable case, for sol 554, d2. Corrected, model spectra are calculated for the three z_0's and two effective measuring heights. ⋆–⋆ is the measured spectrum. For the model spectra, the symbols for the z_0's are: ○ 0.3 cm, □ 1.0 cm, △ 3.0 cm. Solid symbols indicate a height, z, of 0.93 m while open symbols indicate a height of 1.61 m.

Bibliographic Data Sheet **Risø–R–701(EN)**

Title and author(s)

The Boundary Layer of Mars: Fluxes, Stability, Turbulent Spectra and Growth of the Mixed Layer

Lars Landberg, Søren E. Larsen and James E. Tillman

ISBN	ISSN
87–550–1915–3	0106–2840
Dept. or group	Date
Meteorology and Wind Energy	July 1995
Groups own reg. number(s)	Project/contract No.

Pages	Tables	Illustrations	References
54	6	43	38

Abstract (Max. 2000 char.)

Spectra of wind, from high frequency measurements in the Martian atmospheric surface layer, along with the diurnal variation of the height of the mixed atmospheric surface layer are estimated. Heat and momentum fluxes, and stability, are calculated for early spring, from estimates of the surface temperature and from mean Viking Lander 2 temperatures and winds at 44° N, using similarity theory. The surface temperature estimates are obtained from Mission Operations software, enhanced to improve the sensor temperature measurements. Flow distortion by the lander is also taken into account. The diurnal variation of the mechanically and convectively mixed planetary boundary layer is estimated and sample values are presented. The spectra are compared with model spectra, which have been adjusted to simulate aliasing, and high frequency roll-off, both due to sensor response and the large Kolmorogov length of Mars. The surface layer parameters, including the depth of the mixed layer, are used in the calculation of the model spectra for three surface roughnesses and two measuring heights. The spectral models depend on the surface parameters and the estimated surface temperature, and their agreement with the calculated spectra indicates that the surface layer estimation techniques produce self consistent estimates, both for day and night conditions. This agreement is in spite of the fact that an inertial subrange is virtually absent in the Martian atmospheric surface layer due to the large Kolmogorov length scale. The results show that similarity theory developed for Earth applies to Mars, that the spectral models are universal, and can be applied at heights lower by a factor of three than in prior terrestrial applications. They also demonstrate that it is possible to estimate the effects of severe aliasing of wind measurements, and filtering by sensor and atmospheric processes, to produce a model which agrees well with the measured spectra. These results suggest that z_0 probably lies between 1.0 and 3.0 cm and that the value can be significantly refined by further analyses.

Descriptors INIS/EDB

BOUNDARY LAYERS, MARS PLANET, PLANETARY ATMOSPHERES, SPECTRA, TEMPERATURE MEASUREMENT, TIME-SERIES ANALYSIS, TURBULENCE, VELOCITY, WIND

Available on request from:
Information Service Department, Risø National Laboratory (Afdelingen for Informationsservice, Forskningscenter Risø)
P.O. Box 49, DK–4000 Roskilde, Denmark
Phone (+45) 46 77 46 77, ext. 4004/4005 · Telex 43 116 · Fax (+45) 46 75 56 27